

## Contract Information

### FINAL REPORT

|                        |   |
|------------------------|---|
| Contract Number        | N000140-91-10-0-0   |
| Title of Research      | Nanoengineered Surfaces for High Flux Thin Film Evaporation   |
| Principal Investigator | Evelyn N. Wang ( <a href="mailto:enwang@mit.edu">enwang@mit.edu</a> )<br>Department of Mechanical Engineering |
| Organization           | MIT<br>77 Mass Ave. 3-461B, Cambridge MA 02139  |
| Sponsoring Agency      | Office of Naval Research<br>Program Manager: Dr. Mark Spector<br>875 N Randolph St Arlington, VA 22217        |
| Date                   | July 15, 2013<br>Grant Duration: 6/01/09-3/4/13   |

## Technical Section

### *Technical Objectives*

The objective of the work was to investigate nanoengineered surfaces that could modulate the wetting and phase change processes to enhance heat transfer performance. Phase change processes, associated with the large latent heat, have been widely used in applications where high heat fluxes and high heat transfer coefficients are desired. One example is thermal management which has become a critical bottleneck for the advancement of a variety of important defense, space, and commercial systems. Current state-of-the-art cooling approaches have significant limitations, particularly for high heat flux applications. Two-phase fluidic cooling systems, utilizing liquid-vapor phase-change absorbs large fluxes with minimal changes in device temperature [1-3], has been considered as one of the most promising approach to address the demands for thermal management. While efforts have focused primarily on boiling flows in microchannels, liquid-vapor instabilities during phase-change in these systems lead to local dry-out, non-uniform temperature distributions, and significant decreases in critical heat flux [4-8]. Despite extensive research, there remain significant hurdles in the implementation of this technology. In contrast, two-phase jet impingement and spray cooling techniques have been investigated to a much lesser extent, even though such a methods promise high heat transfer coefficients ( $>100 \text{ W/cm}^2\text{K}$ ) with high heat dissipation capability ( $>1000 \text{ W}$  and  $>1000 \text{ W/cm}^2$ ) *via* thin film evaporation [1, 9]. The implementation has comparable challenges. Previous experimental attempts have typically led to pool boiling due to chamber flooding, or liquid dry-out due to insufficient liquid supply [1, 10]. These undesired effects significantly decreased heat transfer coefficients and heat removal rates. In one aspect of this work, we took advantage of state-of-the-art nanoengineering capabilities to address these challenges. We obtained fundamental understanding of the complex fluidic and thermal transport processes on nanoengineered surfaces to realize the great potential of thin film evaporation.

Other than liquid-vapor phase-change, we also explored modification of surface wettability to enhance condensation heat transfer. Dropwise condensation, where the condensate forms discrete droplets rather than continuous films covering the substrate, is considered as one of the most effective approaches to enhance the heat transfer coefficient. Previous work has demonstrated the application of nanostructured superhydrophobic surfaces where condensate can be spontaneously removed *via* a surface-tension-driven mechanism [11]. However, the nucleation density on these surfaces is relatively low since the phase change process relies on high energy active sites to initiate nucleation at low supersaturations, limiting the overall heat transfer performance. Furthermore, air pockets trapped beneath the droplets during growth

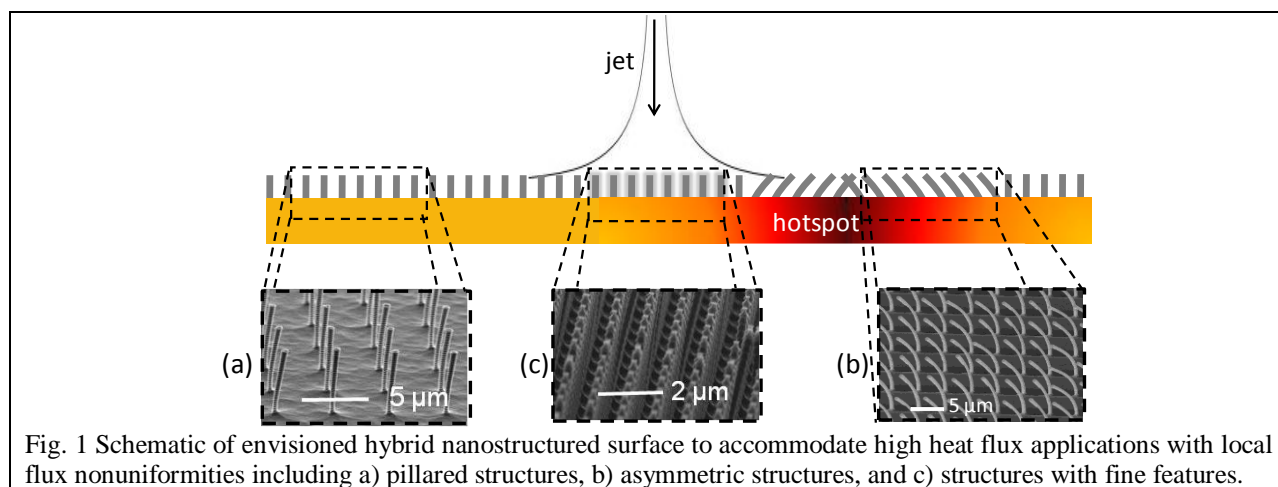
| Report Documentation Page  |                                    |                                     | Form Approved<br>OMB No. 0704-0188                               |   |                                    |
|--|------------------------------------|-------------------------------------|--|---|------------------------------------|
| Public reporting burden for the collection of information is estimated to average 1 hour per response, including the time for reviewing instructions, searching existing data sources, gathering and maintaining the data needed, and completing and reviewing the collection of information. Send comments regarding this burden estimate or any other aspect of this collection of information, including suggestions for reducing this burden, to Washington Headquarters Services, Directorate for Information Operations and Reports, 1215 Jefferson Davis Highway, Suite 1204, Arlington VA 22202-4302. Respondents should be aware that notwithstanding any other provision of law, no person shall be subject to a penalty for failing to comply with a collection of information if it does not display a currently valid OMB control number. |                                    |                                     |  |   |                                    |
| 1. REPORT DATE<br><b>15 JUL 2013</b>   |                                    | 2. REPORT TYPE                      |  | 3. DATES COVERED<br><b>00-00-2009 to 00-00-2013</b> |                                    |
| 4. TITLE AND SUBTITLE<br><b>Nanoengineered Surfaces for High Flux Thin Film Evaporation</b>  |                                    |                                     |  | 5a. CONTRACT NUMBER                                 |                                    |
|  |                                    |                                     |  | 5b. GRANT NUMBER                                    |                                    |
|  |                                    |                                     |  | 5c. PROGRAM ELEMENT NUMBER                          |                                    |
| 6. AUTHOR(S)   |                                    |                                     |  | 5d. PROJECT NUMBER                                  |                                    |
|  |                                    |                                     |  | 5e. TASK NUMBER                                     |                                    |
|  |                                    |                                     |  | 5f. WORK UNIT NUMBER                                |                                    |
| 7. PERFORMING ORGANIZATION NAME(S) AND ADDRESS(ES)<br><b>MIT, 77 Mass Ave. 3-461B, Cambridge, MA, 02139</b>  |                                    |                                     |  | 8. PERFORMING ORGANIZATION<br>REPORT NUMBER         |                                    |
| 9. SPONSORING/MONITORING AGENCY NAME(S) AND ADDRESS(ES)  |                                    |                                     |  | 10. SPONSOR/MONITOR'S ACRONYM(S)                    |                                    |
|  |                                    |                                     |  | 11. SPONSOR/MONITOR'S REPORT<br>NUMBER(S)           |                                    |
| 12. DISTRIBUTION/AVAILABILITY STATEMENT<br><b>Approved for public release; distribution unlimited</b>  |                                    |                                     |  |   |                                    |
| 13. SUPPLEMENTARY NOTES  |                                    |                                     |  |   |                                    |
| 14. ABSTRACT   |                                    |                                     |  |   |                                    |
| 15. SUBJECT TERMS  |                                    |                                     |  |   |                                    |
| 16. SECURITY CLASSIFICATION OF:  |                                    |                                     | 17. LIMITATION OF<br>ABSTRACT<br><b>Same as<br/>Report (SAR)</b> | 18. NUMBER<br>OF PAGES<br><b>35</b>                 | 19a. NAME OF<br>RESPONSIBLE PERSON |
| a. REPORT<br><b>unclassified</b>   | b. ABSTRACT<br><b>unclassified</b> | c. THIS PAGE<br><b>unclassified</b> |  |   |                                    |

reduce the contact area between the condensing droplet and substrate, which increases the thermal resistance and reduces the heat transfer coefficient [12]. In this work, we demonstrated that by infusing hydrophobic oil into superhydrophobic surfaces, the nucleation density was significantly increased while maintaining easy droplet removal. Such a surface could potentially be the ideal surface for condensation heat transfer.

### Technical Approach

Fig. 1 shows the envisioned hybrid nanostructured surface to accommodate high heat flux applications with local flux nonuniformities. Based on our preliminary findings [13, 14], the features include:

- Pillared structures (Fig. 1a) that serve as capillary wicks where the height, spacing, and distribution control the rate of liquid propagation;
- Asymmetric structures (Fig. 1b) that can maneuver the direction of liquid propagation. In the presence of a hotspot where the local flux is higher, the structures direct more liquid towards the region for enhanced heat removal;
- Structures with fine features (Fig. 1c) to allow three-dimensional control and variations in liquid film thickness.



A key step to the realization of the functional surface envisioned in Fig. 1, however, is a systematic investigation and fundamental understanding of the fluid-structure-heat interaction and rich interfacial phenomena within these complex configurations. The goal of our work was to fabricate well-controlled and new nanostructure geometries, and pursue a series of experiments and modeling work to determine how various parameters (shape, size, and spacing, *etc.*) of the nanostructured features affect the coupled heat and mass transport processes. The understanding gained from this work combined with the parametric studies provided new functionalities and offered important steps towards the fine control necessary to achieve the highest cooling capability with thin film evaporation.

### Summary of Achievements

Through the duration of the research grant, we have made several contributions:

1. We developed a predictive model for liquid propagation rates based on the diameter, height, and period of micropillar arrays, which is validated with experiments. This model offers an important step towards optimizing pillar designs to achieve high flux thin film evaporation.
2. We demonstrated that the liquid droplets could exhibit non-wetting behavior on superhydrophilic microstructured surfaces at superheated conditions. Vapor is generated by surface heating and

accumulates beneath the droplet before flowing through the pillar arrays and the increased pressure of vapor supports the droplet on top of silicon micropillar arrays in a non-wetting state. Such non-wetting state is unfavorable for thin film evaporation. A force balance model was developed to delineate the wetting from the non-wetting regime of droplets based on the droplet size and the pillar-array geometry. This study is important in outlining conditions to avoid non-wetting of liquids in thin film evaporation.

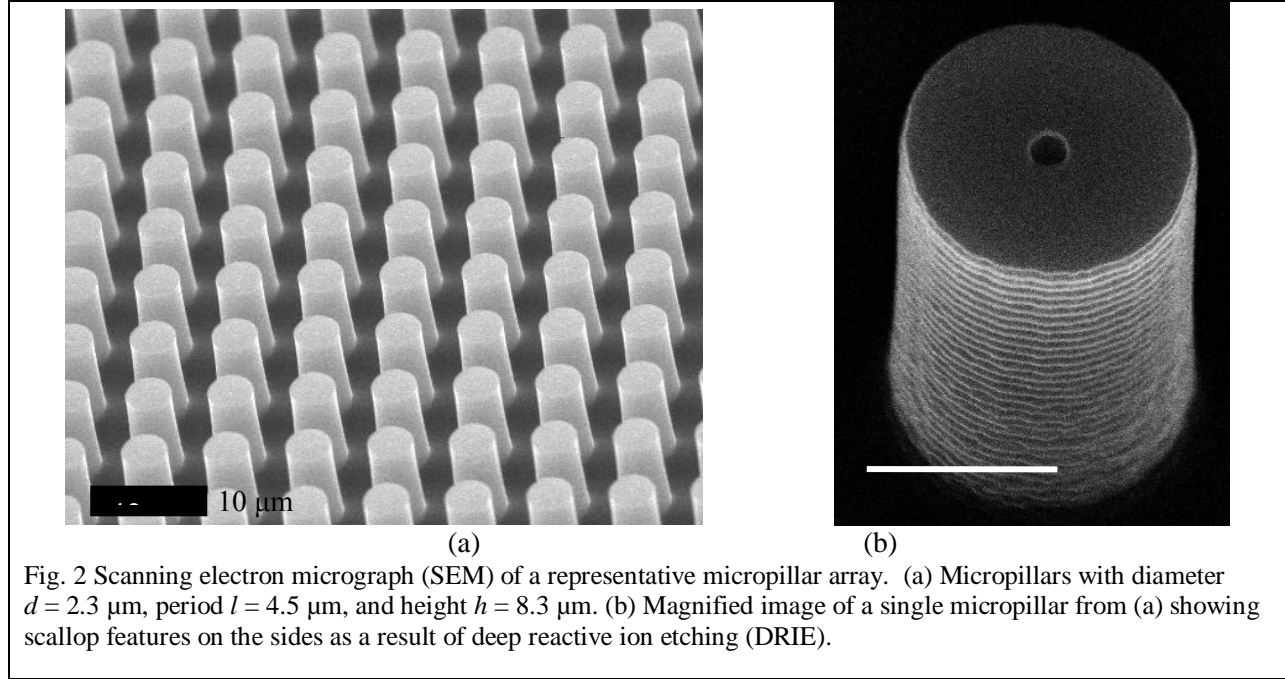
3. We developed a new metrology technique, Pulsed Evaporative Transient Thermometry (PETT), to obtain both the instantaneous heat capacity and heat transfer conductance, *i.e.*, the product of the heat transfer coefficient and surface area, during liquid evaporation from micro and nanostructures. This approach experimentally captures the transient thermal response as the liquid evaporates from micro and nanostructures by a series of applied heat pulses, and uses a lumped system model to extract these two quantities. We demonstrated the applicability of PETT to capture the evaporation process for two model systems, copper microwires and nanoporous alumina membranes with a coated metal film. This PETT technique promises to be a valuable quantitative approach to fundamentally investigate the relationship between wetting morphology and heat transfer behavior for a variety of micro and nanostructured devices.
4. We demonstrated using nanoporous membranes to achieve thin film evaporation over large areas. Steady and transient heat transfer coefficient over  $10^4$  W/m<sup>2</sup>K was obtained with isopropyl alcohol (IPA) as the coolant, which is higher than that of pool boiling and is less than two orders of magnitude smaller than the theoretical limit. This work offers insights into optimal experimental designs towards achieving kinetic limits of heat transfer for thin film evaporation based thermal management solutions.
5. We showed that the nucleation density on oil-infused, silane-coated structured surfaces can be significantly increased by the use of disordered long-chain silane coatings that result in nucleation sites limited only by the density of pillar structures comprising the surface. We find that the increase in the nucleation density can be explained by heterogeneity in the surface energy of the silane coating and the reduced water-oil interfacial energy. This effect could potentially be used to significantly improve the heat transfer coefficient in condensation by controlling the nucleation density.

## **Detailed contributions**

### **1) Liquid Propagation on Micropillar Arrays**

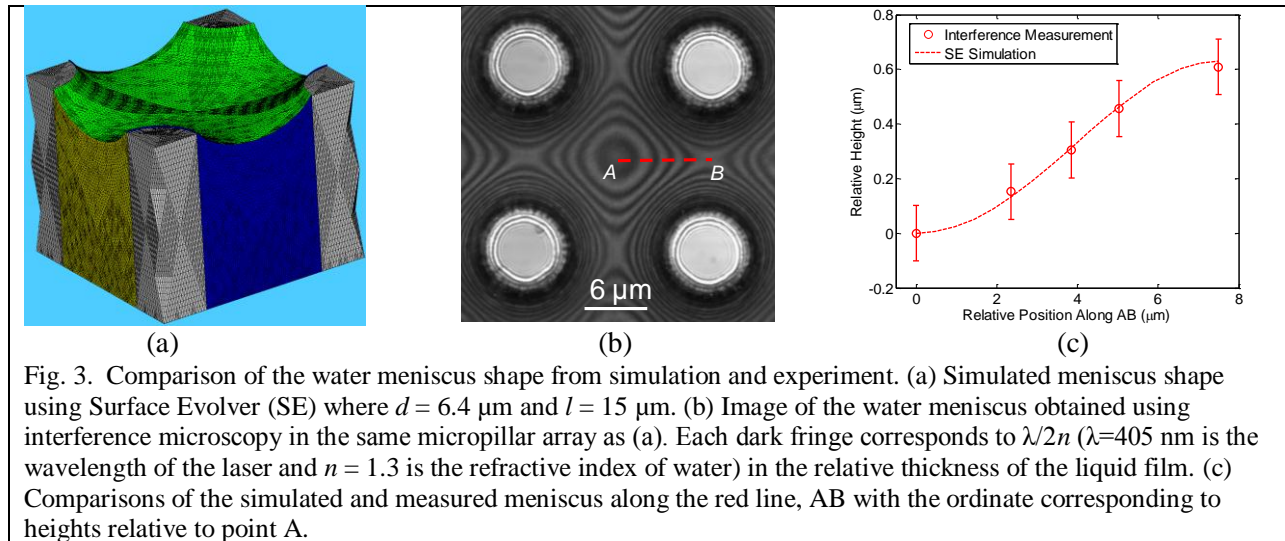
Nanostructures with novel functionalities provide unique opportunities to achieve the desired fluidic control to enhance heat transfer performance. We have successfully fabricated nanostructured surfaces that can manipulate liquids in desired directionalities. However, to successfully design surfaces for optimized heat transfer, we need to obtain quantitative understanding of liquid dynamics on engineered surfaces that can maneuver the liquid and provide the necessary liquid flow rates to avoid dry-out. We have initially focused our studies on uniformly spaced micropillar arrays, which we determined to be complex and rich of interfacial phenomena. We developed a predictive model for liquid propagation rates based on the diameter, height, and period of micropillar arrays, which is validated with experiments. This model offers an important step towards optimizing pillar designs to achieve high flux thin film evaporation.

We have fabricated a range of micropillar arrays with various geometries. The pillar diameters ranged from  $d = 1.3 - 6.4 \mu\text{m}$ , the periods ranged from  $l = 4.5 - 30 \mu\text{m}$ , and the heights ranged from  $h = 8.3 - 20 \mu\text{m}$ . An example of a uniform square array of cylindrical pillars with diameter  $d = 2.3 \mu\text{m}$ , period (pillar center-center distance)  $l = 4.5 \mu\text{m}$ , and height  $h = 8.3 \mu\text{m}$ , is shown in Fig. 2(a). The pillars were defined by photolithography and etched by deep reactive ion etching (DRIE) in silicon. Due to the alternating etch and passivation steps characteristic of DRIE, scallop features were formed on the sides of the pillars (Fig. 2 (b)).



The developed model determines the liquid propagation rate in the pillar arrays based on the balance between the capillary pressure and the viscous resistance following Washburn dynamics. We determined the capillary pressure in the micropillar array using a thermodynamic approach minimizing interfacial free energy. The pressure is defined as the change in surface energy per unit volume,

$$P_{cap} = \Delta E / \Delta V, \quad (1)$$



where  $\Delta E$  is the decrease in surface energy as the liquid fills one unit cell and  $\Delta V$  is the corresponding volume of the liquid filling one unit cell. To accurately predict the change in surface energy and volume, Surface Evolver (SE)[15] was used to simulate the shape of the meniscus with minimum surface energy. A unit cell consisting of four quarter-pillars filled with water was defined as shown in Fig. 3(a). The effect of the scalloped features were included in the simulations as an effective surface energy where the scallops were approximated as a series of semi-circles with a roughness factor,  $rf = \pi/2$ [16]. The intrinsic contact angle of de-ionized (DI) water on the silicon surface was measured by a goniometer to be  $\theta = 38^\circ$ . Geometries with diameters,  $d$ , and periods,  $l$ , ranging from  $2 \mu\text{m}$  to  $8 \mu\text{m}$  and from  $8 \mu\text{m}$  to  $15 \mu\text{m}$ , respectively, were considered.

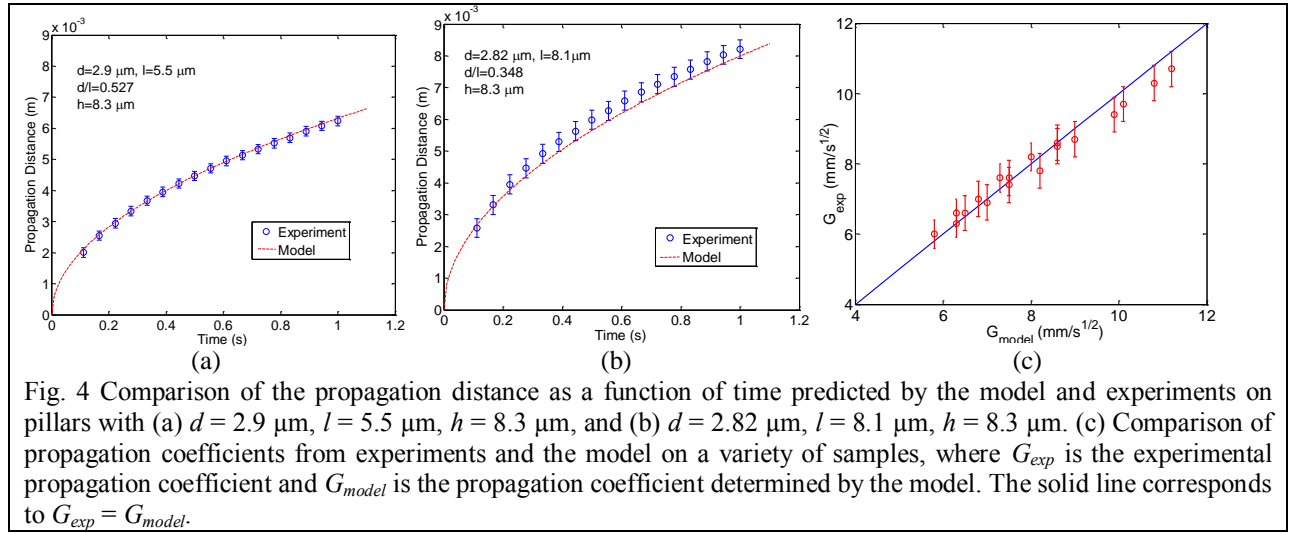
Fig. 3 compares the simulated meniscus shape to experimental interference measurements on a micropillar array with diameter  $d = 6.4 \mu\text{m}$  and period  $l = 15 \mu\text{m}$ . Fig. 3(a) shows the three-dimensional meniscus shape obtained by SE and Fig. 3(b) shows the top-down view of the experimentally obtained interference patterns on the same pillar geometry. Close to the pillar sidewalls ( $< 1 \mu\text{m}$ ), accurate data was difficult to obtain due to refraction. Fig. 3(c) compares the meniscus shape predicted by simulation and obtained experimentally along the horizontal (AB) direction. The error bars in the data were determined based on the width of the dark fringes. The experimental results were well-predicted by the simulation. Based on the excellent agreement between simulations and experiments, SE was used to obtain general correlations for the volume of the liquid,  $\Delta V$ , and the area of the menisci,  $A_m$ . With the prediction of meniscus shape, the capillary pressure can be obtained as

$$P_{cap} = \frac{\Delta E}{\Delta V} = \frac{\gamma \cdot rf \cos \theta \cdot \pi dh + \gamma \cos \theta (l^2 - \pi d^2 / 4) - \gamma A_m}{\Delta V}, \quad (2)$$

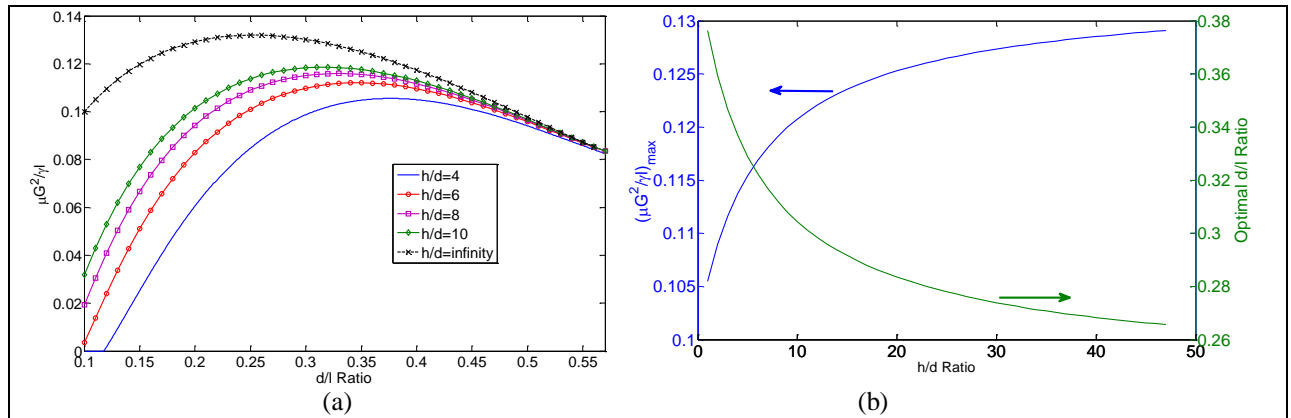
where  $\gamma$  is the surface tension of the liquid,  $\theta$  is the intrinsic contact angle, and  $rf$  is the roughness factor on the sides of the pillars. The first and second term represent the energy change as the liquid wets the sides of the rough pillar and the smooth bottom surface of the unit cell, respectively. The third term corresponds to the energy change due to the formation of the meniscus.

However, we observed in our experiments that two distinct time scales exist in the propagation process and vary as functions of the geometry. The time required for the liquid front to sweep from one pillar to the bottom of the next pillar is defined as  $\tau_s$  and the time required for the liquid front to climb and wet the side of a pillar is defined as  $\tau_p$ . When  $h \geq l$ ,  $\tau_s$  and  $\tau_p$  are comparable, such that the averaged approach described above to determine capillary pressure is accurate. On the other hand, when  $h < l$ , the two time scales start to deviate from each other where  $\tau_s$  becomes dominant. In addition, slight variations in pillar diameter and local wettability become important. In such cases, Eqn (2) is no longer sufficient to describe the driving capillary pressure. We plan to further these investigations in the subsequent year to obtain a comprehensive understanding of the behavior in this regime. However, these sparse pillar geometries are seldom practical, where a large propagation rate is often desired.

Subsequently, we determined the viscous resistance of liquid flow in micropillar arrays using Brinkmann's equation, which is a modified form of the Navier-Stokes equation with a permeability term widely used in porous media studies. The permeability of planar pillar arrays was obtained using the numerical results by Sangani and Acrivos for  $d/l < 0.57$  [17]. Conveniently, pillar arrays with  $d/l$  greater than 0.57 are less commonly used in practice due to the large viscous losses associated with such densely packed arrays. Finite element simulations were carried out and compared to our model and show agreement to within 5%.



From these studies, a model for liquid propagation rates was developed, and verified with one-dimensional propagation experiments. Comparisons between the propagation distance as a function of time from our model and experiments are shown in Fig. 4(a) for  $d = 2.9 \mu\text{m}$ ,  $l = 5.5 \mu\text{m}$ , and  $h = 8.3 \mu\text{m}$ , and Fig. 4 (b) for  $d = 2.82 \mu\text{m}$ ,  $l = 8.1 \mu\text{m}$ , and  $h = 8.3 \mu\text{m}$ . Error bars were obtained by repeating experiments on each sample at least three times. Experiments were also performed on a variety of samples with  $d = 1.8 - 5.3 \mu\text{m}$ ,  $l = 4.5 - 15 \mu\text{m}$ , and  $h = 8.3 - 25 \mu\text{m}$ . Fig. 4 (c) compares the propagation coefficients,  $G$ , from experiments and the model, which are in excellent agreement to within 5%.



We subsequently developed a dimensionless effective propagation rate an effective propagation coefficient,  $\mu G^2/\gamma l$ , was obtained that is functionally dependent on only the dimensionless geometrical parameters  $h/d$  and  $d/l$ , where  $\mu$  is the viscosity of the liquid,  $G$  is the propagation coefficient, and  $\gamma$  is the surface tension. Fig. 5(a) shows the relationship for water on silicon pillars with various  $d/l$  and  $h/d$  ratios. The relationship is valid with  $h \geq l$  and  $d/l < 0.57$ . The effective propagation coefficient can be interpreted as a competition between the viscous resistance and the driving capillary pressure. As the ratio of  $h/d$  increases, the effective propagation coefficient increases and approaches an upper theoretical limit as  $h \rightarrow \infty$ . When the ratio of  $d/l$  increases, the viscous resistance and the capillary pressure both increase and

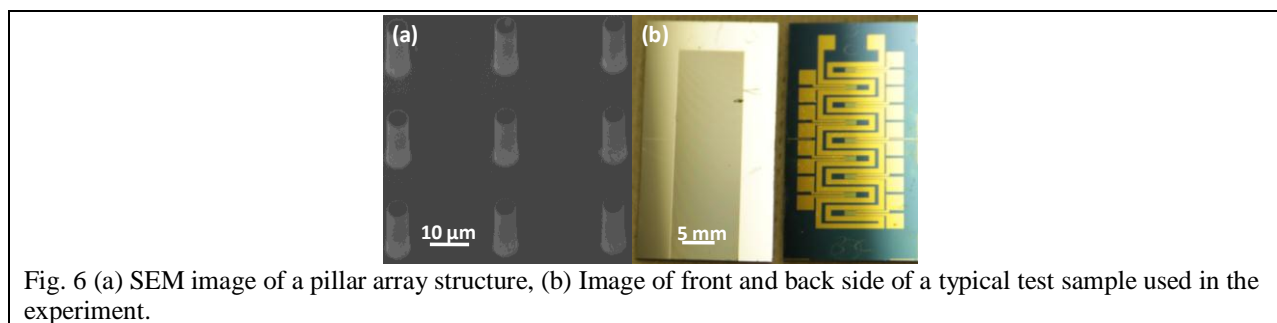


a maximum effective propagation coefficient is reached. Beyond this limit, the viscous resistance increases faster than the capillary pressure, leading to a decrease in the effective propagation coefficient. The optimal  $d/l$  ratio and the corresponding maximum effective propagation coefficient for varying  $h/d$  ratios are shown in Fig. 5 (b). The outcomes of the work show that a maximum effective propagation rate can be achieved by optimizing micropillar geometries.

## 2) Evaporation-Induced Non-Wetting Droplets on Superhydrophilic Surfaces

We discovered during our experiments that liquid droplets could exhibit non-wetting behavior on superhydrophilic microstructured surfaces at superheated conditions. Such a non-wetting state is unfavorable for thin film evaporation and therefore, we investigated the detailed mechanism for this behavior and outlined the conditions to avoid non-wetting of liquids in thin film evaporation.

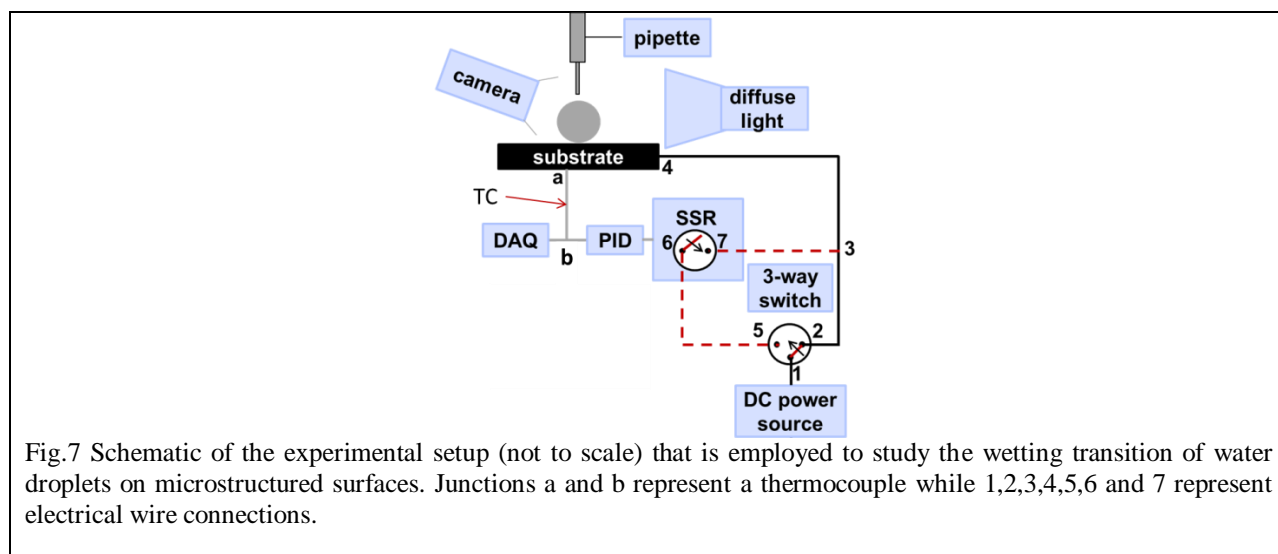
We studied a square array of pillars with  $d = 5.3 \mu\text{m}$ ,  $h = 21.7 \mu\text{m}$ ,  $l = 27.5 \mu\text{m}$ , roughness ratio  $rf = 1.48$ , and solid fraction  $\phi_s = 0.03$ . An SEM image of the microstructured surface at  $30^\circ$  inclination is shown in Fig. 6a. The geometry was chosen such that the imbibition condition [18, 19] was met.



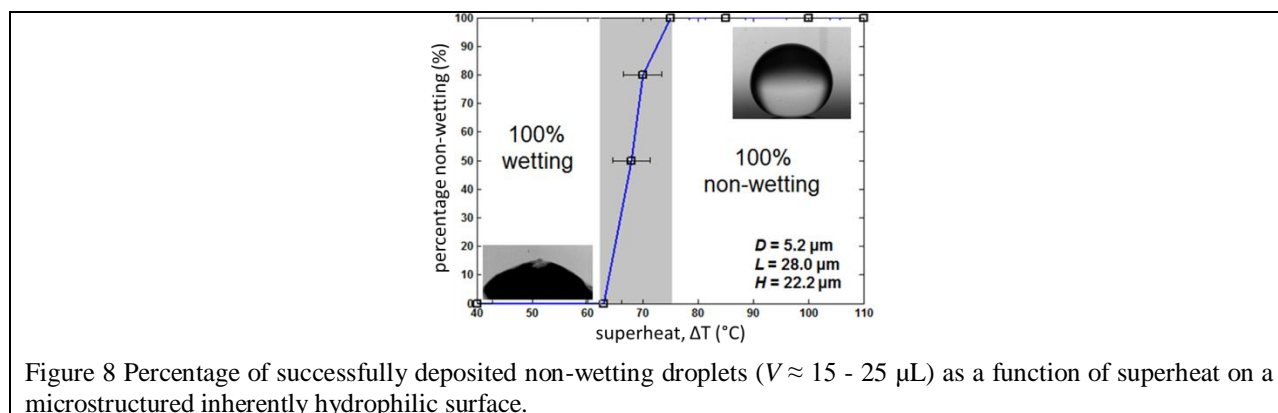
A gold resistive heater (Fig. 6b) was patterned onto the backside of the silicon sample using ebeam evaporation and acetone lift-off processes. A DC power source was used to heat the sample and the temperature was measured at a rate of 10 Hz using a T-type thermocouple (TC) attached to the backside of the test sample using thermal grease (3G Cool Silver, AI Technology) and Kapton tape. Before each experiment, the samples were cleaned with acetone, methanol, isopropanol and deionized (DI) water; dried with nitrogen gas; and then oxygen plasma treated for 30 minutes to remove organic contaminants. After the plasma cleaning procedure, the surface was observed to be superhydrophilic and droplets spontaneously spread upon the surface with near zero contact angle. Thoroughly degassed DI water was used for all experiments to avoid gas bubble nucleation. A pipette was used to gently dispense droplets with volumes between 15 and 25  $\mu\text{L}$  on the heated substrate. A 25  $\mu\text{m}$  diameter gold wire, functionalized in a 1 mM ethanol solution of 1H, 1H, 2H, 2H-perfluorodecanethiol (Sigma-Aldrich), was used to keep the highly mobile droplets in position for visualization.

The superheat required to deposit a non-wetting droplet on top of the microstructured surface was observed to be higher than that required to sustain the non-wetting state of an already deposited droplet. This necessitated a strategy that would allow the substrate to be maintained at two different steady state superheats: a higher superheat initially and a relatively lower superheat after droplet deposition. This was achieved using a PID controller as shown in the schematic circuit setup shown in Fig. 7 where the substrate was initially heated directly through 1-2-3-4 to establish the first higher steady state superheat and through 1-5-6-7-3-4 to establish the second lower steady state superheat. The second steady state superheat is achieved by toggling a 3-way switch from 2 to 5 such that the PID controls the heating power by utilizing a closed loop temperature feedback system.





In order to visualize the droplet behavior and understand the mechanism involved during wetting transition, images were acquired at 10 fps which are later synchronized with the temperature data to extract the parameters of interest. The droplet volume, diameter and apparent contact angle were calculated by processing the captured images through a custom analysis routine written in MATLAB<sup>®</sup>. To investigate whether or not a water droplet wets a microstructured surface or not at a specified superheat, ten droplets were deposited on the surface. The result is shown on Fig. 8 where the percentage of non-wetting droplets obtained out of ten experiments is shown at each superheat. All droplets deposited below 63 °C superheat wetted the surface while non-wetting droplets formed at all times when the superheat was kept higher than 75 °C. Between 63 °C and 75 °C superheat, a droplet could be in either wetting or non-wetting state depending on how gently it was deposited on the surface [20]. However, the probability of depositing a non-wetting droplet monotonically increased as the superheat increased.



A typical experiment detailing the experimental methodology is shown in Fig. 9. A steady state superheat of 94 °C was required to initially deposit a non-wetting droplet while only 26 °C was necessary to sustain the non-wetting state of an already deposited droplet. The wetting transition occurred at 26 °C, 35.1 s after deposition.

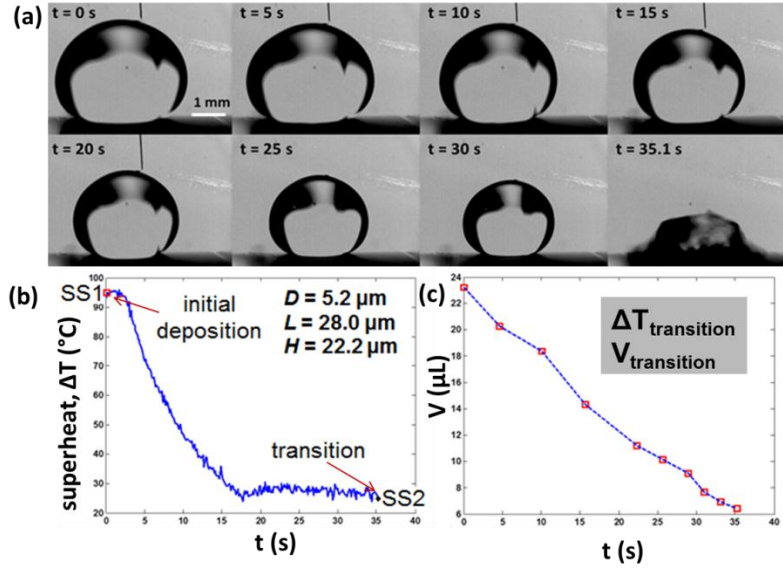


Fig. 9 (a) Typical time lapse images of an evaporating droplet on a microstructured surface at 5 s intervals, (b) superheat as a function of time, (c) corresponding droplet volume as a function of time.

To explain the observations, we developed a simple quasi-steady 1-D lubrication model which is valid after steady state superheat was achieved ( $>18$  s on Fig. 9b). A schematic of an evaporating droplet on top of the structured surface is shown on Fig. 10. The temperature at the droplet base (or pillar top) is assumed to be the saturation temperature of water at ambient pressure. Uniform evaporation throughout the droplet base was assumed. The apparent contact angle of the droplet was estimated using the Cassie-Baxter equation for composite surfaces [21, 22], a porous silicon pillars and water vapor in this case,

$$\cos \theta_c = -1 + \phi_s(1 + \cos \theta_f), \quad (3)$$

where,  $\theta_f$  and  $\theta_c$  are the intrinsic contact angle on a smooth surface and the apparent contact angle respectively

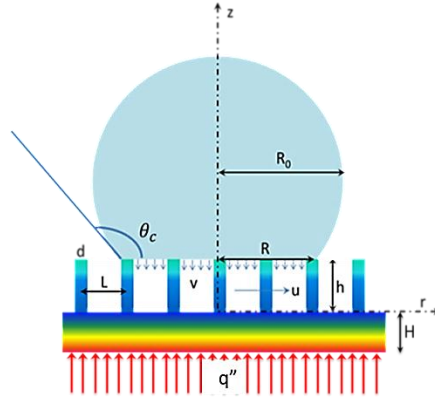


Fig. 10 Schematic of a non-wetting droplet on a superheated microstructured surface. Heat is conducted through the substrate and the porous pillar-vapor media to induce evaporation at the three-phase contact line.

We further assume that the conducted heat is completely utilized to induce uniform evaporation at the liquid-vapor interface of the droplet basal area. The vapor escapes from the droplet base with velocity  $v$  in the  $z$ -direction and could be related to the heat conduction through the composite media as

$$v = -\frac{k_{eff}\Delta T_p}{\rho_{vap}h_{fg}h'} \quad (4)$$

where  $\rho_{vap}$  and  $h_{fg}$  are the density of vapor and the latent heat of vaporization respectively,  $\Delta T_p$  is the temperature difference between the pillar top and the pillar base, and  $k_{eff}$  is the effective thermal conductivity of the porous media composed of the silicon pillars and the water vapor and is estimated by Eq. 3 from [23]

$$k_{eff} = (1 - \phi_s)k_{vap} + \phi_s k_{si}, \quad (5)$$

where  $k_{vap}$  and  $k_{si}$  are the thermal conductivities of water vapor and silicon at saturation conditions ( $k_{si}$  at 100 °C is approximately 105 W/m.k) [24].

Considering that  $h/R \ll 1$ , it is assumed that the vapor velocity  $v$  in the  $z$ -direction is small compared to the radial vapor velocity  $u$ . The continuity equation at any radial position under the droplet base can then be equated with Eq. 5 to give

$$\int_0^h u \, dz = -\frac{k_{eff}\Delta T_p}{2\rho_{vap}h_{fg}} \frac{r}{h}. \quad (6)$$

Further assumptions can be made that simplify the analysis as follows: (1) the viscous loss is dominated by velocity gradients in the  $z$ -direction, (2) momentum changes in the axial direction can be neglected, and (3) the pressure depends only in the radial direction. The above assumptions reduce the momentum equation for porous media to Brinkman equation [25],

$$\frac{\partial^2 u}{\partial z^2} = \frac{\varepsilon}{\mu} \frac{dP}{dr} + \frac{\varepsilon u}{K}, \quad (7)$$

where  $\varepsilon$  is the porosity and  $K$  is the permeability of the porous media (unit  $m^2$ ). The permeability was calculated using an asymptotic expression valid for flow through dilute pillar arrays,  $\phi_s \leq 0.25$  [26]. Equation 7 is then solved by applying the no-slip boundary conditions at the pillar base and pillar top. An average radial velocity, which depends only on the radial direction, can then be found by integrating the velocity profile from the pillar base to the tip. This average radial velocity is then equated with the average velocity obtained previously from Eq. 6 to find the pressure profile along the radial direction which gives rise to the upward anti-wetting force on the droplet  $F_{anti-wet}$  which is given by

$$F_{anti-wet} = \frac{\pi \varepsilon \mu_{vap} k_{eff} \Delta T_p}{8 \rho_{vap} h_{fg}} \left( \frac{2 \tanh\left(\frac{h}{2} \sqrt{\frac{\varepsilon}{K}}\right)}{\left(\frac{\varepsilon}{K}\right)^{3/2}} - \frac{hK}{\varepsilon} \right)^{-1} \frac{R^4}{h}. \quad (8)$$

The downward wetting force on the droplet  $F_{wet}$  due to the weight of the droplet and the surface tension is given by

$$F_{wet} = \rho_{liq} V g + N \pi d \sigma \cos \theta_f, \quad (9)$$

where  $V$  is the droplet volume,  $\rho_{liq}$  is the density of liquid water at saturation temperature,  $d$  is the pillar diameter, and  $N = \pi R^2 / l^2$  is the number of pillars in contact with the droplet base. The force due to surface tension is the dominant wetting force, and hence the scaling  $F_{wet} \propto R^2$ . On the other hand the anti-wetting force scales as  $F_{anti-wet} \propto R^4$ . Hence, due to evaporation, the anti-wetting force decreases faster than the wetting force. The superheat required to suspend a droplet on top of the pillar array can be obtained by equating the two competing forces,

$$\Delta T_p = \frac{\rho_{liq} V g + \sigma \pi N d \cos \theta_f}{\frac{\pi \varepsilon \mu_{vap} k_{eff}}{8 \rho_{vap} h_{fg}} \left( \frac{2 \tanh \left( \frac{h}{2} \sqrt{\frac{\varepsilon}{K}} \right)}{\left( \frac{\varepsilon}{K} \right)^{3/2}} - \frac{h K}{\varepsilon} \right)^{-1} \frac{R^4}{h}}. \quad (10)$$

Equation 10 estimates the superheat between the pillar base and pillar top that is required to suspend a droplet. An additional temperature drop between the pillar base and the backside of the substrate is required to match the experimentally measured wall temperature with the model prediction. Incorporating this additional temperature drop across the sample thickness ( $H \sim 620 \mu\text{m}$ ), the overall temperature drop from the backside of the sample to the pillar top is

$$\Delta T = \Delta T_p \left( 1 + \frac{H k_{eff}}{h k_{si}} \right). \quad (11)$$

Equation 11 provides an estimate for the overall superheat  $\Delta T$  required to suspend a droplet on top of a microstructured surface. The superheat increases as the droplet decreases in size ( $\Delta T \propto R^{-2}$ ), consistent with experimental observations. A typical experimental data and the model prediction are shown in Fig. 11. The simple 1-D lubrication type model qualitatively captures the transition mechanism and shows a good agreement between experimental data and model prediction.

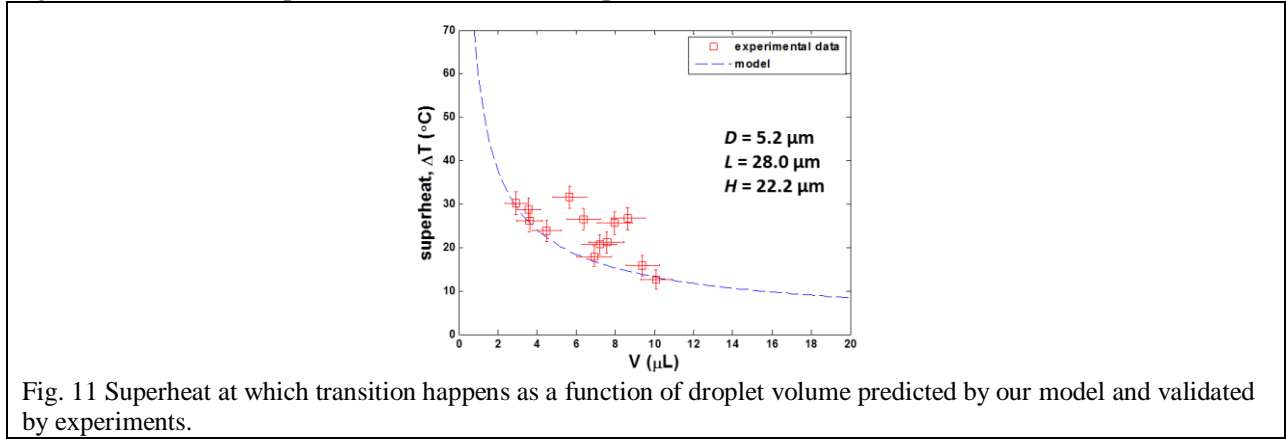


Fig. 11 Superheat at which transition happens as a function of droplet volume predicted by our model and validated by experiments.

In summary, we demonstrated that a superhydrophilic surface at room temperature can take on the characteristics of a superhydrophobic surface if the substrate is superheated beyond a critical superheat. Experiments performed at steady state conditions on superhydrophilic surfaces have shown that a relatively smaller superheat is required to sustain an already suspended non-wetting droplet than that required when initially depositing the droplet. We have also demonstrated experimentally that a single surface can exhibit both extremes of wettability: superhydrophilicity and superhydrophobicity. The 1-D lubrication type model developed shows good agreement with experimental data. This work offers new insights into the design of structured surfaces for phase-change heat transfer applications that seek high heat flux removal.

### 3) Pulsed Evaporative Transient (PETT) for Temporally-resolved Thermal Property Measurement

Previous studies have showed that the heat transfer performance of thin film evaporation is highly dependent on the microscale liquid film morphology. Numerical simulations have compared the heat transfer performance of different microstructures for thin film evaporation [27]. Meanwhile, various experimental approaches have been used to study the relationship between meniscus shape and heat transfer behavior, such as infrared [28], and interference imaging [29]. However, these previous experimental investigations were generally steady state or slowly varying measurements where a constant

heat flux was applied and a steady-state temperature was measured. Accordingly, the average heat transfer coefficient was determined over a long period of time ( $O(\text{mins})$ ) and compared with imaging results. While these approaches are of practical merit where the actual application may desire steady-state performance, to fundamentally understand the correlation between the heat transfer coefficient and the liquid film morphology, a temporally-resolved measurement over the duration of the evaporation process is of interest.

We developed a new metrology technique, Pulsed Evaporative Transient Thermometry (PETT), to obtain both the instantaneous heat capacity and heat transfer conductance, *i.e.*, the product of the heat transfer coefficient and surface area, during liquid evaporation from micro and nanostructures. This approach experimentally captures the transient thermal response as the liquid evaporates from micro and nanostructures by a series of applied heat pulses, and uses a lumped system model to extract these two quantities. We demonstrated the applicability of PETT to capture the evaporation process for two model systems, copper microwires and nanoporous alumina membranes with a coated metal film. In the case of the copper microwires (diameters  $\approx 20 \mu\text{m}$ ), we obtained transient heat transfer conductances with a temporal resolution of 1 second and captured the peak heat transfer conductance at the thin film stage of  $1.3 \times 10^{-4} \text{ W/K}$ , *i.e.*,  $\approx 4\times$  as high as the dry surface ( $3.2 \times 10^{-5} \text{ W/K}$ ). In addition, we showed that the heat transfer behavior were distinct between the oxidized and un-oxidized surfaces, which correlated well with microscopic visualizations of the droplet evaporation process. For the nanoporous membranes, a higher temporal resolution of 0.2 seconds was achieved owing to the significantly higher heat transfer conductance. In addition, a peak in the heat transfer conductance greater than  $1.2 \text{ W/K}$  during the evaporation process was recorded, which corresponds to the thin film evaporation state with the smallest liquid film thickness. This PETT technique promises to be a valuable quantitative approach to fundamentally investigate the relationship between wetting morphology and heat transfer behavior for a variety of micro and nanostructured devices.

The experimental setup for PETT is shown in Fig. 12a. For this technique, there are two pre-requisites required for the test microdevice: 1) The Biot number of the device ( $Bi = hA/kL$ , where  $hA$  is the heat transfer conductance,  $k$  is the thermal conductivity, and  $L$  is the characteristic thickness of the device) needs to be low ( $<0.1$ ) so that the device can be treated as a lumped system; and 2) The device needs to have a finite resistance which varies with temperature, such that the average temperature of the device can be measured using the change in resistance. This test device is connected to a reference resistor, which is stable against temperature change, and a function generator, which provides electrical pulses. After wetted by liquid, the microdevice is heated by applying a series of pulses while the thermal response from the resistance change is captured by a DAQ system. The experimental data is then combined with the lumped model to extract the heat capacity of the system and the heat transfer conductance described as follows.

When the device is heated by a pulse, the temperature response is determined by

$$\frac{d(\Delta T)}{dt} + \frac{hA}{C} \Delta T = \frac{P}{C} \quad (12)$$

where  $hA$  is the heat transfer conductance with  $h$  being the heat transfer coefficient and  $A$  the surface area,  $C$  is the heat capacity of the microdevice, and  $P$  is the heating power.

By solving Eqn (12), the temperature difference,  $\Delta T$ , as a function of time,  $t$ , is given as

$$\Delta T = \frac{P}{hA} [1 - e^{-\frac{hA}{C}t}]. \quad (13)$$

In the case of microdevices made from metal or coated with metal, the resistance varies linearly with temperature. Accordingly, the change in resistance can be expressed as

$$\Delta R = \frac{\alpha P R_0}{hA} [1 - e^{-\frac{hA}{C}t}] \quad (14)$$

where  $\alpha$  is the temperature coefficient of resistivity and  $R_0$  is the initial resistance of the device.

Therefore, the temporally-resolved resistance of the microdevice is determined by the heat transfer conductance,  $hA$ , together with the heat capacity,  $C$ . Note that typically, the heat transfer conductance of the system is the useful quantity to determine performance, however the heat transfer coefficient can be determined if the surface area of the microdevice can be accurately determined. Fig. 12b shows two typical responses with copper microwires (diameter of 20  $\mu\text{m}$ , resistance of  $\approx 10\ \Omega$ ) heated by pulses with a magnitude of 600 mV and a duration of 0.2 seconds with water droplets evaporating from the surface. As the droplets evaporate, the heat transfer conductance changes, which results in a change in the resistance response. Meanwhile, the heat capacity of the system can be obtained using the response at the early stage ( $t \ll \frac{hA}{C}$ ), where the change in the resistance can be determined as

$$\Delta R \approx \frac{\alpha P R_0}{hA} \cdot \frac{hA}{C} t = \frac{\alpha P R_0}{C} t \quad (15)$$

As a result, the change in the resistance is approximately linear with time and the slope indicates the heat capacity as shown in Fig. 12c.

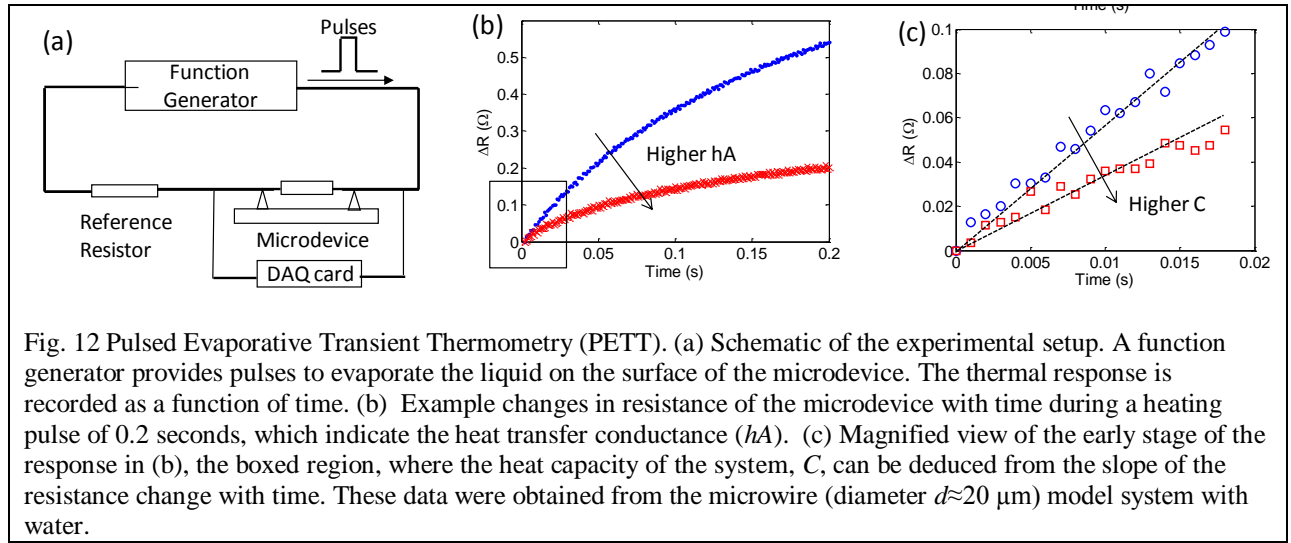


Fig. 12 Pulsed Evaporative Transient Thermometry (PETT). (a) Schematic of the experimental setup. A function generator provides pulses to evaporate the liquid on the surface of the microdevice. The thermal response is recorded as a function of time. (b) Example changes in resistance of the microdevice with time during a heating pulse of 0.2 seconds, which indicate the heat transfer conductance ( $hA$ ). (c) Magnified view of the early stage of the response in (b), the boxed region, where the heat capacity of the system,  $C$ , can be deduced from the slope of the resistance change with time. These data were obtained from the microwire (diameter  $d \approx 20\ \mu\text{m}$ ) model system with water.

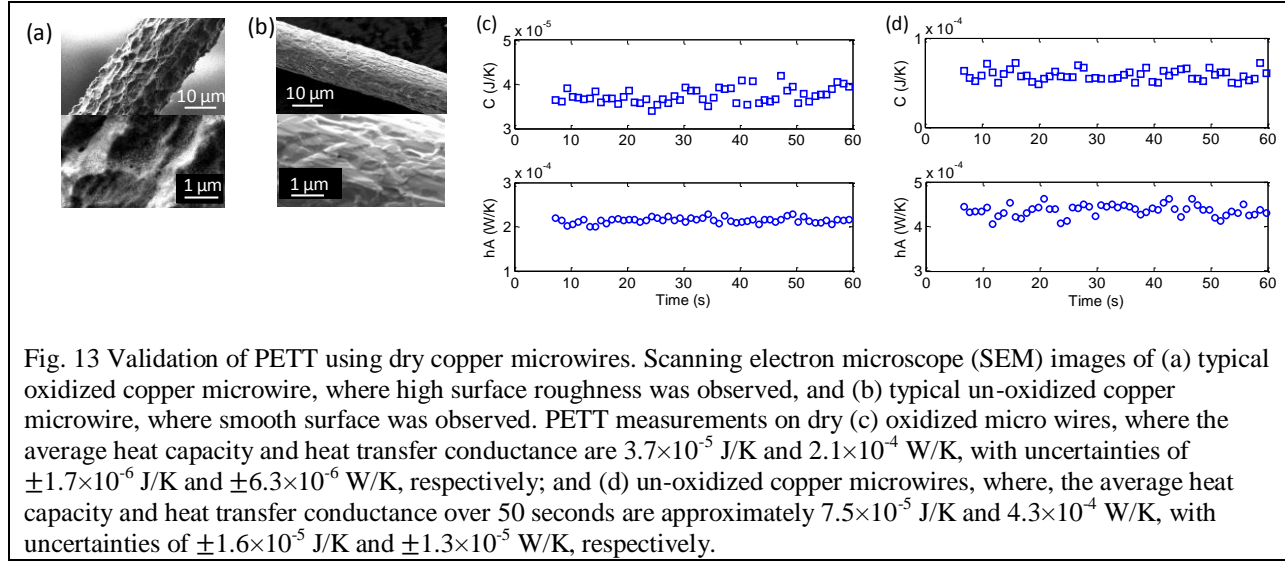
Note that in the model, the heating power was assumed to be constant to achieve the ideal exponential response. In actual experiments, a constant heating power is difficult to implement. Instead, a constant voltage is applied to the reference resistance and the microdevice. However, by matching the reference resistance and the resistance of the test device, the variation in the heating power can be minimized as shown below

$$\frac{dP}{dT} = \frac{d}{dT} \left[ \left( \frac{U}{R_f + R} \right)^2 R \right] = \frac{dR}{dT} \frac{U^2}{(R_f + R)^2} \left( 1 - \frac{2R}{R_f + R} \right) \quad (16)$$

where  $R_f$  is the reference resistance and  $U$  is the total voltage. Therefore, by choosing  $R_f \approx R$ , the variation in the heating power can be neglected and the proposed model will accurately capture the experiments.

We first used copper microwires as a model system to demonstrate the capability of the PETT technique, where we examined the difference in evaporation behavior and corresponding heat transfer conductances on oxidized and un-oxidized microwires. Copper wires were procured (McMaster Carr) with diameters of 76  $\mu\text{m}$ , and were subsequently etched by iron(III) chloride solution, decreasing the diameter to  $\approx 20\ \mu\text{m}$ , and increasing the electrical resistance of the sample to the range of 10-30  $\Omega$ . With these resistance values, a simple 2-wire configuration could be used to achieve accurate resistance measurements. After etching, we oxidized some of the copper microwires to effectively increase the hydrophilicity of the

copper surface [30]. The scanning electron microscope (SEM) images of the oxidized surfaces are shown in Fig. 13(a). The oxidation process significantly enhanced both the micro and nanoscale roughness of the microwire in comparison with the un-oxidized microwires in Fig. 13(b).



The microwires were placed into the experimental setup in Fig. 12. PETT measurements were first obtained on dry microwires to validate the method and determine the uncertainty of the results. The temporally resolved heat capacity and heat transfer conductance on dry oxidized and un-oxidized copper wires are shown in Fig. 13(c) & (d), respectively. On oxidized microwires, the average heat capacity and heat transfer conductance over 50 seconds were approximately  $3.7 \times 10^{-5}$  J/K and  $2.1 \times 10^{-4}$  W/K, with uncertainties of  $\pm 1.7 \times 10^{-6}$  J/K and  $\pm 6.3 \times 10^{-6}$  W/K, respectively. On un-oxidized microwires, the average heat capacity and heat transfer conductance over 50 seconds were approximately  $7.5 \times 10^{-5}$  J/K and  $4.3 \times 10^{-4}$  W/K, with uncertainties of  $\pm 1.6 \times 10^{-5}$  J/K and  $\pm 1.3 \times 10^{-5}$  W/K, respectively. The uncertainties were one order of magnitude smaller compared to the average values, indicating good consistency and reliability. Note that the measured heat capacity and heat transfer conductance on the un-oxidized wires were  $\approx 2\times$  of that on the oxidized wire. This was due to the fact that the oxidized wires used in the tests were approximately half the length of the un-oxidized ones. We chose the different lengths in experiments for practical reasons. Ideally, the wires should be as long as possible so that the electrical resistance can be large for easier measurements. However, during the oxidation process, the samples were placed in the oxidation solution with agitation. Long wires with such small diameters ( $\approx 20$   $\mu\text{m}$ ) tended to break more easily due to agitation. Therefore, we reduced the lengths of the wires for oxidation.

Afterwards, we wetted the surface with water and captured the evaporation process without heating using a CMOS camera (Phantom V7.1, Vision Research Inc.) at a frame rate of 10 frames per second through a white light microscope (Eclipse LV-100, Nikon) with a  $20\times$  objective (NA = 0.60).



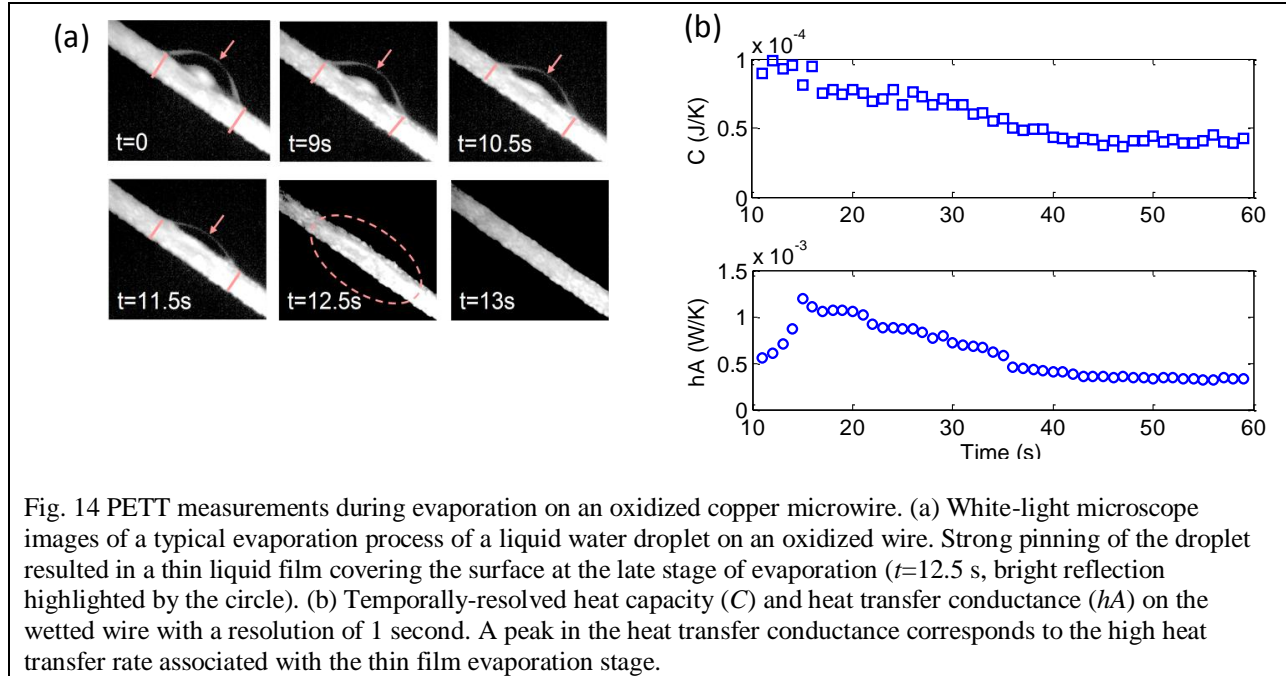


Fig. 14 PETT measurements during evaporation on an oxidized copper microwire. (a) White-light microscope images of a typical evaporation process of a liquid water droplet on an oxidized wire. Strong pinning of the droplet resulted in a thin liquid film covering the surface at the late stage of evaporation ( $t=12.5\text{ s}$ , bright reflection highlighted by the circle). (b) Temporally-resolved heat capacity ( $C$ ) and heat transfer conductance ( $hA$ ) on the wetted wire with a resolution of 1 second. A peak in the heat transfer conductance corresponds to the high heat transfer rate associated with the thin film evaporation stage.

The time-lapse images in Fig. 14(a) show that the liquid droplet was pinned due to the enhanced roughness and hydrophilicity and the thickness of the droplet decreased during the evaporation process. Therefore, at the late stage of the evaporation ( $t=12.5\text{ s}$  in this specific experiment), thin liquid films were formed, as highlighted by the circle in Fig. 14(a). Based on these visualizations, a peak in heat transfer conductance was expected corresponding to this thin film stage. The PETT measurement during an example evaporation experiment is shown in Fig. 14(b). Each heating pulse lasted for 0.2 seconds to achieve a significant increase in resistance. A subsequent 0.8 seconds waiting period between pulses was used in order for the sample to cool to the ambient temperature prior to the next pulse. As a result, the overall temporal resolution was 1 second. The heat capacity,  $C$ , of the device decreased from the initial value of  $\approx 1.0 \times 10^{-4}\text{ J/K}$  as liquid evaporated to a steady dry value of  $\approx 5 \times 10^{-5}\text{ J/K}$  at the end of the experiment. The heat transfer conductance,  $hA$ , increased to reach a peak value of  $\approx 1.3 \times 10^{-3}\text{ W/K}$  and then decreased to the dry value of  $\approx 3.2 \times 10^{-4}\text{ W/K}$  towards the end of the experiment, as expected. Accordingly, the peak heat transfer conductance was  $4\times$  as large as that when the wire was dry.

For comparison, experiments were also carried out on un-oxidized copper microwires with smooth surfaces. Time-lapse images of a representative evaporation process on the un-oxidized wires are shown in Fig. 15(a). Due to the reduced roughness and consequently less pinning of the droplets, the base area of droplets decreased continuously during the evaporation process and the thin film stage was not observed. Therefore, no peak in heat transfer conductance was expected, as confirmed by the temporally-resolved measurement of heat capacity and heat transfer conductance in Fig. 15(b). Similar with the oxidized wires, the heat capacity gradually decreased from  $\approx 1.5 \times 10^{-4}\text{ J/K}$  to  $\approx 7 \times 10^{-5}\text{ J/K}$  as water evaporated. However, the heat transfer conductance also decreased gradually from  $\approx 1.5 \times 10^{-3}\text{ W/K}$  to  $\approx 0.5 \times 10^{-3}\text{ W/K}$  with no peak. The heat transfer behavior was distinctly different between the evaporation processes on oxidized and un-oxidized copper wires due to the difference in surface property and liquid morphology.

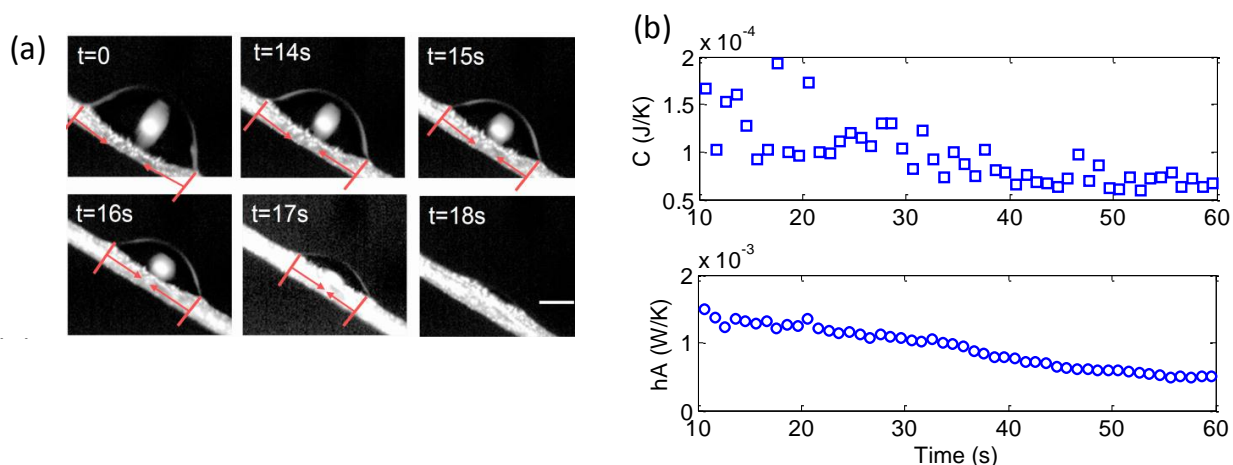


Fig. 15 PETT measurements during evaporation on an un-oxidized copper microwire. (a) White-light microscope images of a typical evaporation process of a liquid water droplet on an un-oxidized microwire. The wetted area shrunk gradually during the evaporation process. (b) Temporally-resolved heat capacity ( $C$ ) and heat transfer conductance ( $hA$ ) on the wetted wire with a resolution of 1 second. There is no peak in the heat transfer conductance because the high heat transfer rate with the thin film evaporation stage was not observed.

Using microwires, we showed that the PETT technique is capable of measuring transient thermal properties. While the microwires offer a convenient platform for fundamental investigations, they are not common configurations for practical applications. Moreover, the low heat transfer conductance requires long cooling period between pulses, which limits the temporal resolution. We further expanded the PETT technique to a more practical configuration for thin film evaporation using nanoporous membranes wetted by isopropyl alcohol. Isopropyl alcohol was used in this case to allow easy wetting of the membrane due to the low surface tension, and to delay electrolysis when in contact with the metal electrode. The large surface area and complete wetting allowed significantly higher heat transfer conductances, which greatly reduce the required cooling period. Therefore, we targeted 0.2 seconds of temporal resolution with a pulse duration of 0.1 seconds and cooling period of 0.1 seconds. As will be discussed in more detail later, however, there is a trade-off between obtaining high temporal resolution and high signal-to-noise ratio.

The average pore diameter of the procured alumina membranes (Synkera Inc.) was 150 nm with a thickness of 100  $\mu\text{m}$ . A 30 nm thick layer of platinum was sputtered onto the membrane surface, which served as both the heater and an area-averaged temperature sensor. Images of the coated membrane are shown in Fig. 16(a). Typical changes in resistance with time responses are shown in Fig. 16 (b) for different heat transfer conductances. Due to the large heat transfer conductance and short pulse introduced, however, the increase in resistance during the pulse ( $<0.04 \Omega$ ) became much smaller compared to that in the microwire configuration ( $>0.2 \Omega$ ). As a result, noise from data acquisition system became much more significant compared to the desired signal.

The temporally-resolved heat transfer conductance measured by PETT is shown in Fig. 16(c). Initially when the membrane was completely wetted and flooded with IPA, the heat transfer conductance was steady around 0.38 W/K. As evaporation occurred, a clear peak in heat transfer conductance was observed prior to dry-out, which corresponds to the stage where the membrane was wetted by a thin liquid film. Later, as the thin liquid film evaporated, the heat transfer coefficient decreased to 0.14 W/K, which is associated with natural convection and conduction loss through the electrical contacts.

The changes in resistance during the peak in heat transfer conductance are shown as the red data points in Fig. 16(b). A curve fit to the data yielded a heat transfer conductance of 3.6 W/K with an increase of

0.006  $\Omega$  in the resistance, which is smaller than the standard deviation of 0.01  $\Omega$ . This fitted result corresponds to an upper bound of heat transfer conductance, plotted in Fig. 16c as a red square. It is possible that the actual increase in the resistance was higher but was masked by the noise. However, the upper bound for the actual increase should be twice that of the standard deviation ( $\leq 0.02$   $\Omega$ ). Based on Eqn (3), the upper bound of the actual resistance increase corresponds to a lower bound in heat transfer conductance, which is  $(hA)_{min} = \frac{\alpha PR_0}{(\Delta R)_{max}} = 1.2$  W/K. This value is also plotted in Fig. 16(c) as a red dot. The lower bound in heat transfer conductance at the peak remains one order of magnitude larger than that at the dry stage. Despite the uncertainty in the actual peak heat transfer conductance, the results indicate that the peak in the thin film evaporation stage exists. Due to the significant noise and small resistance change, however, we were not able to determine the heat capacity.

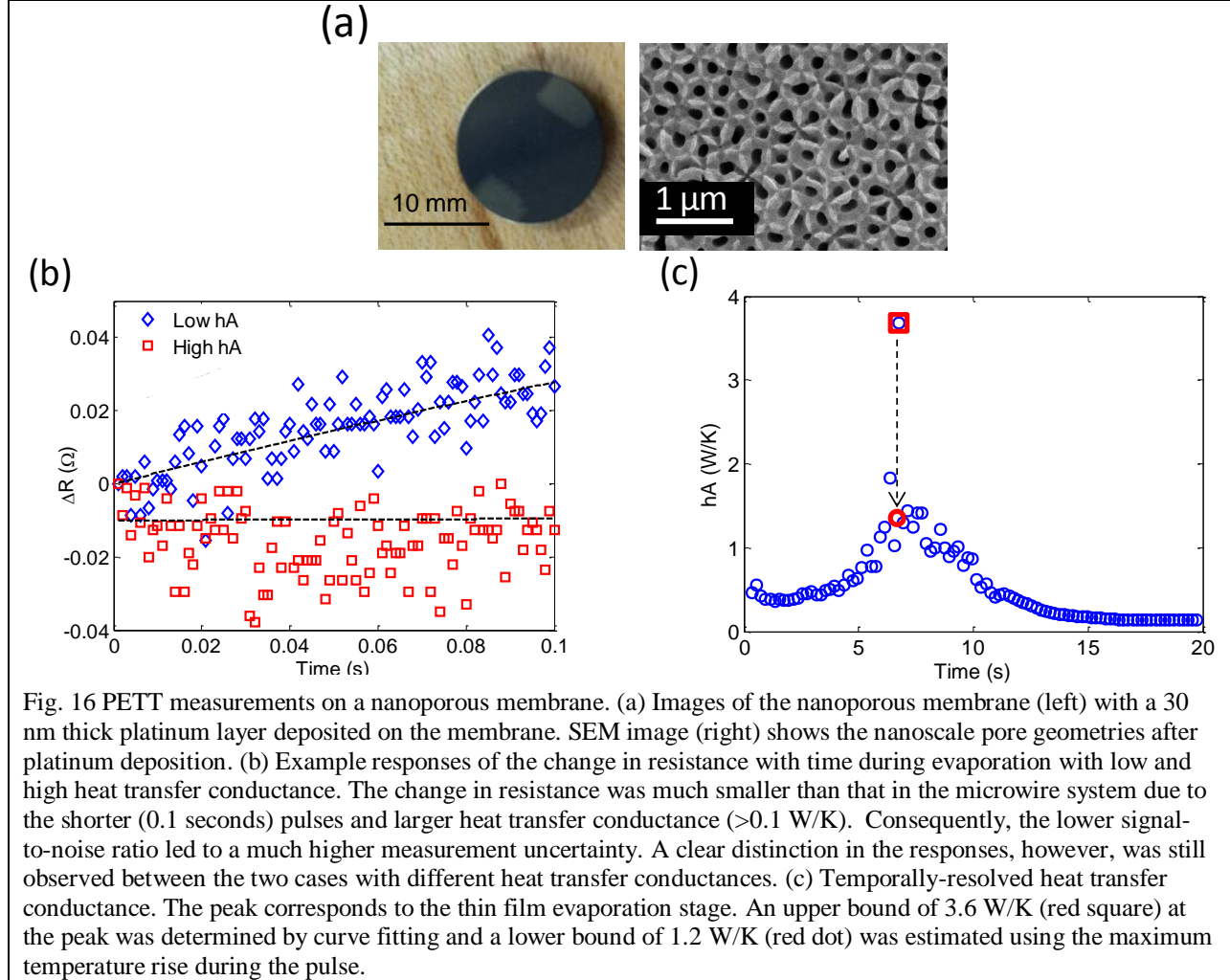


Fig. 16 PETT measurements on a nanoporous membrane. (a) Images of the nanoporous membrane (left) with a 30 nm thick platinum layer deposited on the membrane. SEM image (right) shows the nanoscale pore geometries after platinum deposition. (b) Example responses of the change in resistance with time during evaporation with low and high heat transfer conductance. The change in resistance was much smaller than that in the microwire system due to the shorter (0.1 seconds) pulses and larger heat transfer conductance ( $>0.1$  W/K). Consequently, the lower signal-to-noise ratio led to a much higher measurement uncertainty. A clear distinction in the responses, however, was still observed between the two cases with different heat transfer conductances. (c) Temporally-resolved heat transfer conductance. The peak corresponds to the thin film evaporation stage. An upper bound of 3.6 W/K (red square) at the peak was determined by curve fitting and a lower bound of 1.2 W/K (red dot) was estimated using the maximum temperature rise during the pulse.

Based on the results from the two types of model systems, we show that there are trade-offs in implementing this technique associated with temporal resolution and accuracy. We showed that for systems with high heat transfer conductance (membrane), the cooling period between the applied pulses can be much shorter to achieve improved temporal resolution, but the uncertainty of the results can become significant. Meanwhile, for systems with low heat transfer conductance (microwires), the large increase in resistance allows for higher signal-to-noise ratios and more accurate measurements of transient heat capacity and heat transfer conductance; however, the temporal resolution is limited. Accordingly, the considerations of accuracy and temporal resolution need to be thoroughly considered before determining the proper parameters to implement the PETT technique. In addition, improving the

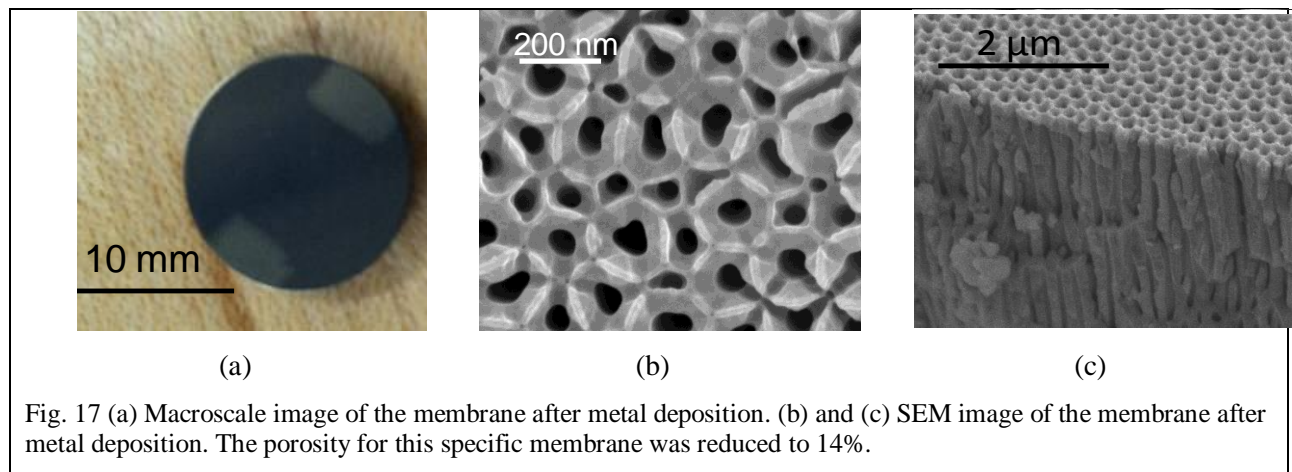
signal to noise ratio in the DAQ system would also be helpful to increase the accuracy of the measurements.

In summary, a new metrology technique, Pulsed Evaporative Transient Thermometry (PETT), was presented to determine instantaneous heat capacity and heat transfer conductance of the system. This technique utilizes short pulses to heat the sample and captures the transient response to extract these quantities. We demonstrated this approach to two model systems of copper microwires with different surface treatments and nanoporous membranes. With different system properties, optimized accuracy and temporal resolution can be achieved by tuning the duration of heating pulses and the cooling period. This approach promises wide application to a variety of micro and nanostructures to improve understanding of phase change heat transfer processes.

#### 4) Thin Film Evaporation from Nanoporous Membranes

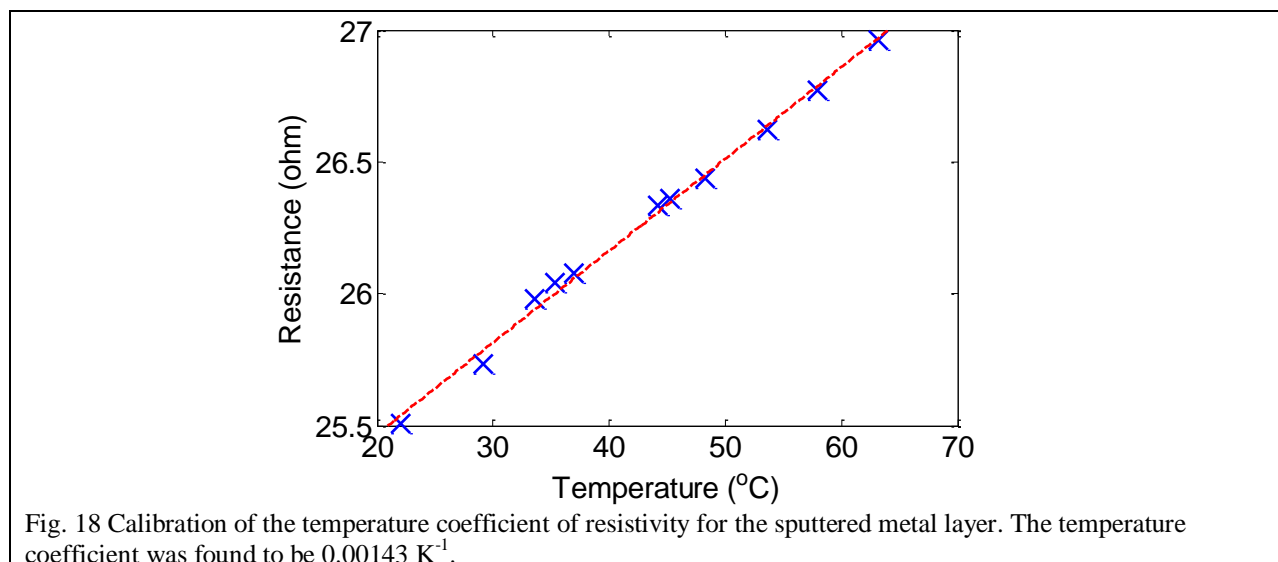
In addition to using microstructured surfaces, we realized upon the course of this study that a nanoporous membrane configuration promises the highest performance. Accordingly, we performed thin film evaporation experiment from nanoporous membranes using isopropyl alcohol (IPA) as the coolant. With average pore diameters of 150 nm, absolute negative pressures as low as  $\approx -300$  kPa were demonstrated. These pressures enabled interfacial heat fluxes of  $\approx 96$  W/cm<sup>2</sup> using IPA as the working fluid. Furthermore, we provide design guidelines to achieve heat fluxes over 1000 W/cm<sup>2</sup> by creating nanoporous membranes with thicknesses on the order of 1  $\mu$ m. This study is a first step towards demonstrating the feasibility of a high performance heat flux device using thin film evaporation.

The nanoporous membranes used in our experiment was anodized aluminum oxide membranes (Unikera, Synkera Inc.) with diameter of 13 mm. The average pore diameter was 150 nm. A 35 nm thick platinum layer was deposited on top of the membrane by sputtering, which was used as resistance heater as well as temperature sensor. The liquid was driven by capillary pressure as well as disjoining pressure through the pores to form the menisci. An example macroscale image and SEM image of the membrane after metal deposition are shown in Fig. 17(a) and (b), respectively. Note that the average pore diameter of 150 nm and porosity of 32% is based on manufacturer's specifications. Based on image analysis of the SEM image after metal deposition, the porosity of this membrane is reduced to 14% by the metal layer. Later, we show that the porosity after metal deposition ranges and needs to be quantified for every batch of fabricated membranes.

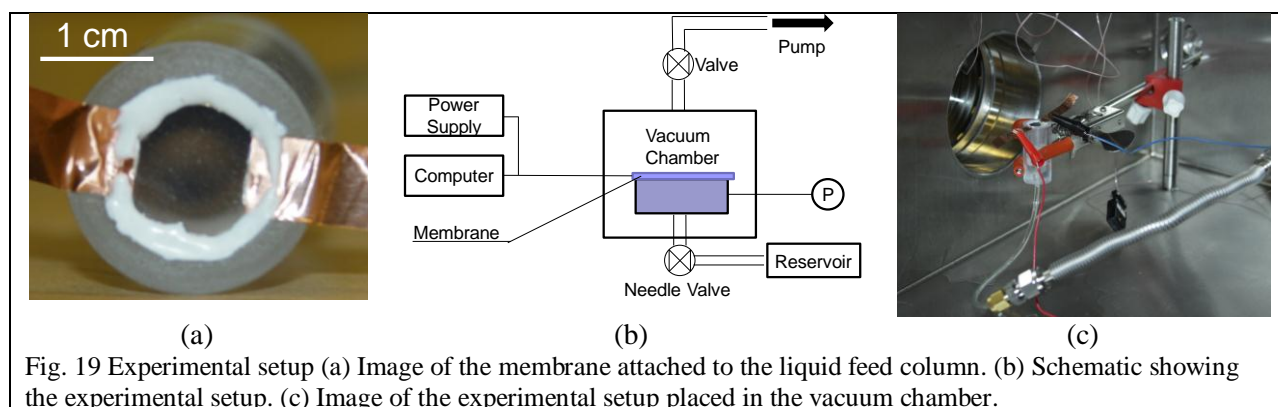


During the experiment, the temperature was measured by the change in the resistance of the metal layer. However, due to the nanoscale geometry of the platinum layer and the sputtering fabrication process, the electrical property of the metal layer is different from that of the bulk material. Therefore, the temperature

coefficient of resistivity was calibrated by an oven and a RTD thermal probe. The result of the calibration is shown in Fig. 18. The temperature coefficient of resistance was found to be  $0.00143 \text{ K}^{-1}$ .



In the experiment, the membrane was attached to a liquid feed column with the edge of the membrane sealed by vacuum epoxy (Torr Seal, Varian Inc.) to ensure that liquid can only transport through the nanopores in the membrane, as shown in Fig. 19(a). The area that can be wetted by the fluid in the membrane is  $0.5 \text{ cm}^2$ . Considering the porosity of 14%, the actual interfacial area available for evaporation is  $0.07 \text{ cm}^2$ . The liquid feed column is placed in a vacuum chamber (Kurt J. Lesker). A vacuum pump removes the vapor generated during evaporation to eliminate the thermal resistance associated with vapor transport. The pressure of the chamber is monitored by a pressure transducer. The bottom of the liquid feed column is connected to a liquid reservoir outside the vacuum chamber at atmosphere. A voltage was supplied to the metal layer to provide the heat fluxes. The voltage and current was measured by multimeters (Multimeter 2001, Keithley) and recorded by a computer using LabView (National Instruments) program such that the total heating power and temperature can be recorded. The data was acquired at a frequency of 1 Hz. The schematic and actual image of the setup is shown in Fig. 19(b) and (c), respectively. At each heating power, the membrane is allowed to reach steady state where the temperature variation is typically lower than 2 degrees over 100 seconds. After that, the heating power is varied to gather more data points.





In the experiments, the heat was dissipated by evaporation, conduction through the fixture, and convection through the liquid. The conduction heat loss through the fixture can be determined by measuring the temperature change as a function of heating power without liquid supply, as shown in Fig. 20. In the test, the chamber was pumped down the actual experiment condition (~60 Pa). The heat loss through the fixture was found to be around 0.01 W/K.

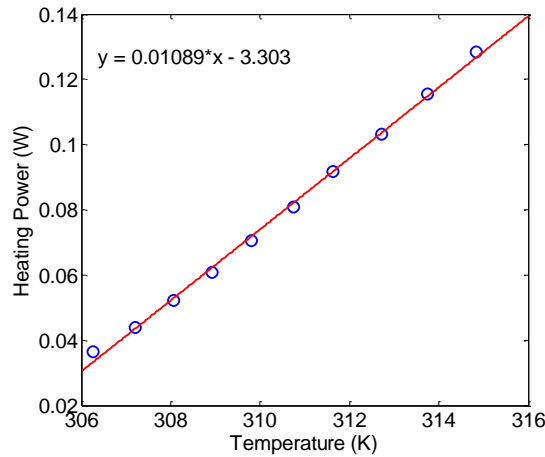


Fig. 20 Temperature of the membrane as a function of heating power without liquid supply. The conduction loss through the fixture was found to be around 0.01 W/K.

The heat loss through convection through the liquid is estimated using the correlation given by Kadambi and Drake for external natural convection of a heated horizontal plate facing down [31]

$$Nu_L = 0.82Ra_L^{1/5} \quad (17)$$

where  $Ra_L$  is the Rayleigh number determined by

$$Ra_L = \frac{g\beta}{\nu\alpha} \Delta T L^3 \quad (18)$$

Given the fluid properties of isopropyl alcohol, the heat loss due to convection can be estimated to be

$$(hA) = 0.006 \text{ W/K} \quad (19)$$

Note that the correlation used here is for external natural convection where the fluid is not confined compared to the practical experiment fixture where the fluid is confined in the feed column. Therefore the calculated heat loss should be an overestimation compared to the actual case.

The typical temperature rise during the experiment is around 30-50 K. Therefore, the maximum total heat loss will be <0.8 W, which is very small compared to the applied heating power.

The variation of the steady state temperature of the membrane with the increase in heat flux is shown in Fig. 21(a). Different symbols indicate different tests, where good consistency was observed. Data was acquired using isopropyl alcohol (IPA) as the coolant. We used IPA instead of water due to the low surface tension of IPA, which allows wetting of the membrane even when the membrane gets contaminated and become less hydrophilic. Future effort will be focused on fabricating surfaces with robust hydrophilicity. As shown in Fig. 21(a), the initial heat transfer coefficient was relatively low with low heat flux. This result is because at the early stage, the liquid flow driven by the pressure difference applied by the vacuum pumping is higher than the evaporation rate. The top surface of the membrane was flooded by the excessive amount of liquid, which introduced a large thermal resistance. As the heat flux was increased, the evaporation rate became higher than the flow rate driven by pressure difference and the excessive amount of liquid on the surface on the membrane evaporated. The heat transfer coefficient increased significantly as the liquid menisci receded back into the pores and formed thin film regions. With further increase in the heat flux, the menisci shape yielded larger thin film regions resulting in the continuous increase of the heat transfer coefficient. At this stage with higher heat transfer coefficient, the

liquid was driven through the pores by a combination of the vacuum pumping pressure, the capillary pressure and the disjoining pressure. However, with further increase in the heat flux, the total driving pressure was no longer able to supply enough liquid for evaporation, and the membrane started to dry out with significant rise of the membrane temperature. The images showing the flooding and the thin film evaporation states of the membrane are shown in Fig. 21(b) and (c), respectively. The heat transfer coefficient of thin film evaporation can be determined as  $1.3 \text{ W/cm}^2\text{K}$  using the slope of the data points in the thin film operating state (dashed line in Fig. 21(a)). Before the drying out occurs, the maximum interfacial heat flux was  $\sim 50 \text{ W/cm}^2$  based on the actual interfacial area of  $0.07 \text{ cm}^2$  at the working temperature of  $345 \text{ K}$ .

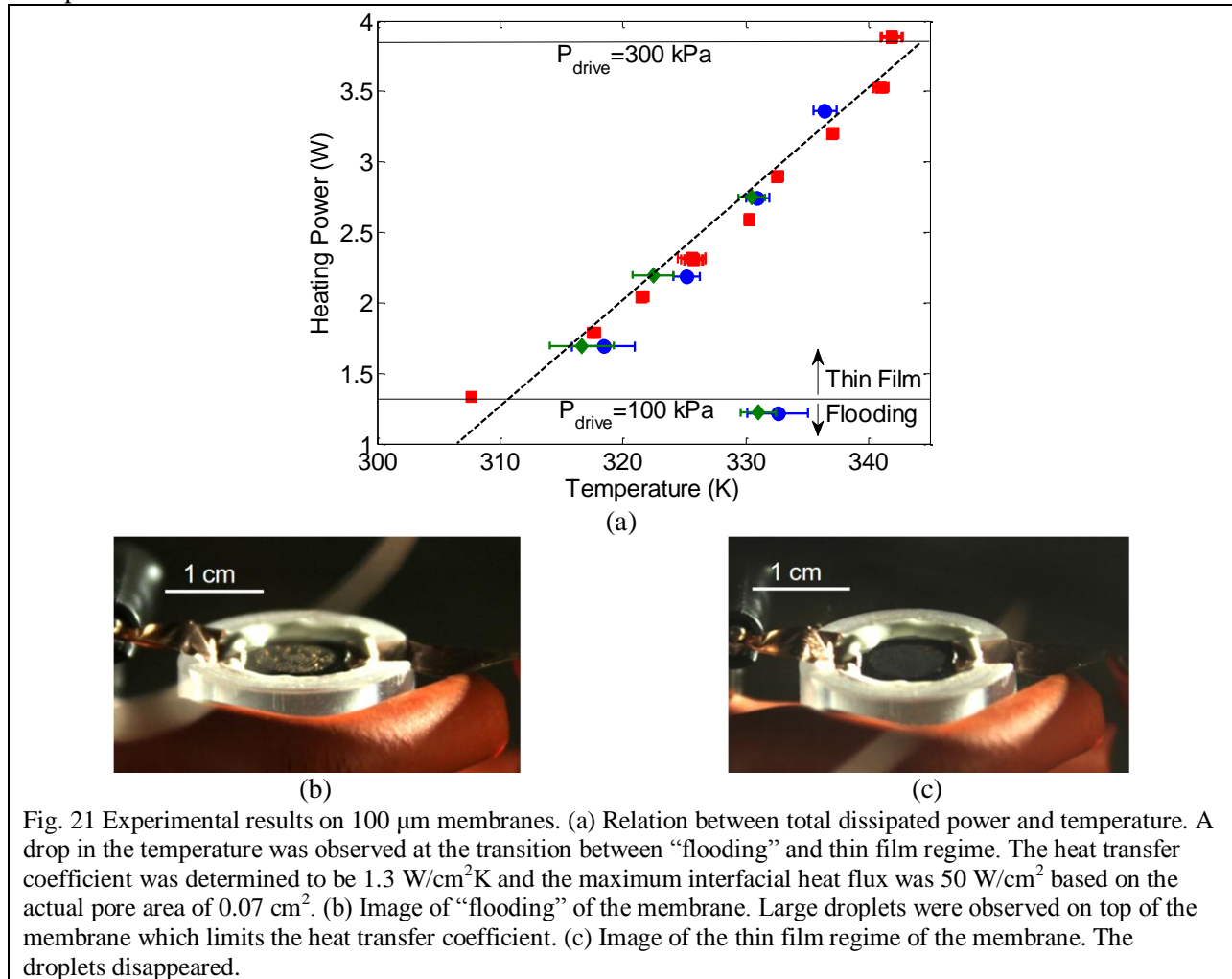


Fig. 21 Experimental results on  $100 \mu\text{m}$  membranes. (a) Relation between total dissipated power and temperature. A drop in the temperature was observed at the transition between “flooding” and thin film regime. The heat transfer coefficient was determined to be  $1.3 \text{ W/cm}^2\text{K}$  and the maximum interfacial heat flux was  $50 \text{ W/cm}^2$  based on the actual pore area of  $0.07 \text{ cm}^2$ . (b) Image of “flooding” of the membrane. Large droplets were observed on top of the membrane which limits the heat transfer coefficient. (c) Image of the thin film regime of the membrane. The droplets disappeared.

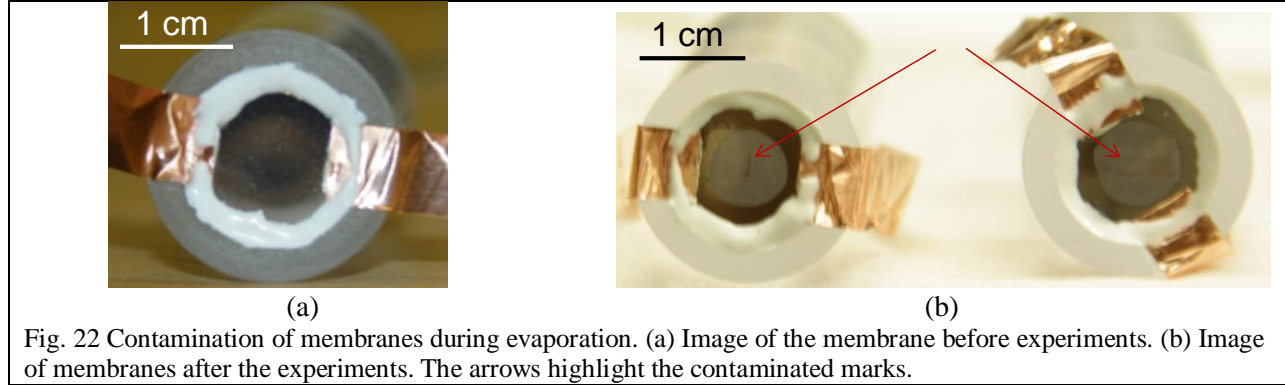
The transition between flooding and thin film evaporation occurred at a heating power of approximately  $1.2\sim 1.3 \text{ W}$ , where the fluid transport through the nanopores is purely driven by the pressure difference (atmospheric pressure,  $\sim 100 \text{ kPa}$ ) across the membrane. While at the dry-out point ( $\sim 3.9 \text{ W}$ ), the fluid is driven by the combination of atmospheric pressure and capillary pressure. Based on energy conservation, the flow rate before the dry-out should be  $3.9/1.3=3$  times as large compared to the flow rate at the transition point between flooding and thin film evaporation. Therefore, the total driving pressure including atmospheric pressure and capillary pressure should be  $\sim 300 \text{ kPa}$ . As a result, the fluid near the meniscus is in negative pressure ( $\sim 200 \text{ kPa}$ ). This negative pressure is allowed by nanoscale confinement of the pores which prevents the cavitation of fluid [32]. Using Young-Laplace equation, the maximum capillary pressure can be estimated as



$$P_{cap} = \frac{2\sigma}{r} = 746 \text{ kPa} \quad (20)$$

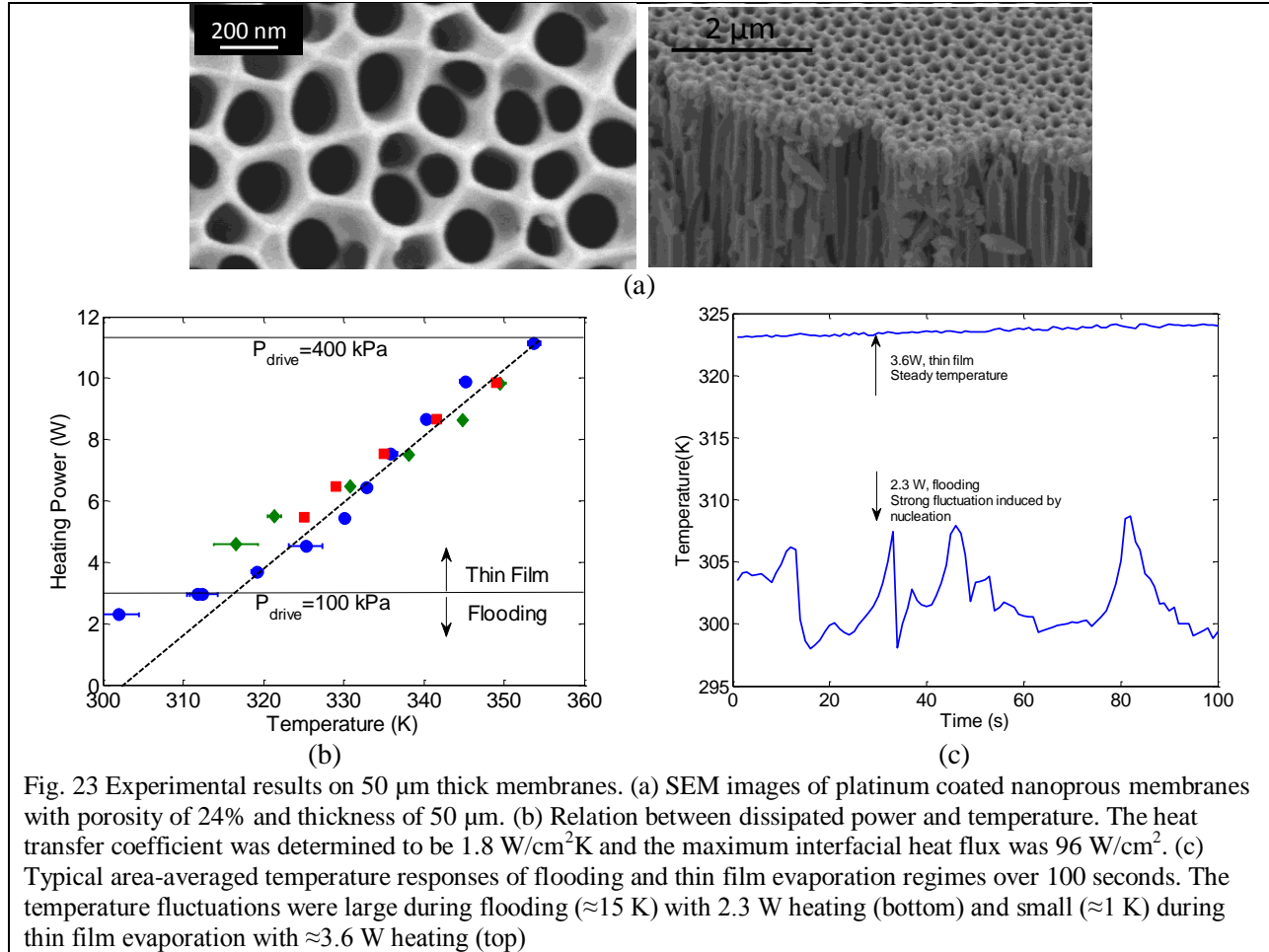
where  $\sigma$  is the surface tension of the liquid ( $\sim 0.019$  at 345K) and  $r$  is the average radius of the pores ( $\sim 50$  nm after metal deposition).

The actual demonstrated capillary pressure is significantly lower than the theoretical limit due to a few reasons. First of all, Young-Laplace equation assumes a circular pore while the actual pores in the membrane are not circular and have a distribution in the pore size, as can be seen in the SEM. Secondly, the fluid used in the experiment is only 99% pure. Significant contamination was observed after the experiment, as shown in Fig. 22(a) and (b). Such contamination reduces the capillary pressure available to drive the liquid transport.



In order to evaluate the demonstrated interfacial heat flux of  $50 \text{ W/cm}^2$ , the critical heat flux (CHF) of IPA in pool boiling was estimated using Kandlikar's model for a benchmark comparison [33]. The CHF is dependent on the orientation of the heated surface and ranges from  $39 \text{ W/cm}^2$  (vertical surface) to  $73 \text{ W/cm}^2$  (horizontal surface). The demonstrated heat flux is comparable with CHF of pool boiling. The major limitation in the heat flux is the supply of fluid. Due to the relatively large thickness ( $100 \mu\text{m}$ ) of the membrane, the viscous resistance of liquid flow through the nanopores is significant. However, assuming a constant driving capillary pressure of 200 kPa and same pore geometries, the maximum heat flux would be inversely proportional to the thickness of the membrane. Therefore, the decoupling between capillarity and viscous resistance and significantly higher heat fluxes can be achieved by reducing the thickness of the membrane.

In order to validate the scaling, experiments using thinner membranes were performed. The thickness of the new membrane is reduced to  $50 \mu\text{m}$ . SEM image of the pore geometries is shown in Fig. 23 (a), by which the porosity after the deposition was determined as 24% and the total pore area is  $0.12 \text{ cm}^2$ . The results are summarized in Fig. 23(b). The pressure in the chamber during the experiment is around 200-300 Pa. Due to the reduced thickness and higher porosity, a much larger amount of fluid can be pushed through the membrane at low heating power to form a liquid pool on top of the membrane where nucleation was observed in contrast to the liquid droplets observed on the  $100 \mu\text{m}$  thick membranes. As a result, significant temperature fluctuation was seen at low heating power which prohibits recording accurate data. Meanwhile, with increased heating power, the flooding can be removed and the temperature becomes stabilized. The comparison between low heating power and high heating power is shown in Fig. 23(b). Therefore, in these experiments, the data points at low heating power are not shown. The transition from flooding and thin film evaporation is determined as the point where the fluctuation in temperature starts to diminish, which is around 2.9 W.



Using the slope of the data points in the thin film region, the heat transfer coefficient can be determined as 1.8  $\text{W}/\text{cm}^2\text{K}$ . Meanwhile, the maximum heating power before dry-out occurs is 11.6 W, yielding an interfacial heat flux of  $11.6/0.12=96$   $\text{W}/\text{cm}^2$ . Therefore the maximum capillary pressure in the nanopores can be determined as  $\sim 300$  kPa using the similar analysis as on 100  $\mu\text{m}$  membranes. The pressure in the liquid near the menisci is  $\sim 300$  kPa. Note that the overall heat flux before dry-out is only  $\sim 23$   $\text{W}/\text{cm}^2$  due to the porosity of 24%. Note that during the experiments, the pressure in the chamber was kept very low (60 Pa $\sim$ 200 Pa) for efficient removal of the vapor to eliminate the thermal resistance associated with vapor transport. Such pressures are significantly lower than the saturation pressure based on the temperature of the membrane. Therefore, the liquid will evaporate due to the low pressure even without heating, called “flashing”. The contribution of flashing can be estimated as follows.

For 100  $\mu\text{m}$  thick membranes, the mass flux driven by the pressure difference without heating will be

$$\dot{m} = \frac{\dot{q}}{h_{fg}} = \frac{1.2}{7.33 \times 10^5} = 1.63 \times 10^{-6} \text{ kg/s} \quad (21)$$

A fraction of this liquid flux will be evaporated while the other part will be cooled from the original temperature of the reservoir (22  $^\circ\text{C}$ ) to the saturation temperature ( $-20$   $^\circ\text{C}$ ) corresponding to the chamber pressure (60 Pa). The sensible cooling of the liquid will provide the latent heat required for evaporation. As a result, the evaporation mass flux,  $m_{evp}$ , will satisfy

$$7.33 \times 10^5 m_{evp} = (22 + 20)(\dot{m} - m_{evp})C_p \quad (22)$$

where  $C_p$  is the specific heat of IPA. Therefore

$$m_{evp} = 2.5 \times 10^{-7} \text{ kg/s}$$

The corresponding heat flux driven by flashing will be

$$q_{flh} = 2.62 \text{ W/cm}^2$$

which is ~ 5% of the total maximum interfacial heat flux with heating.

For the 50  $\mu\text{m}$  thick membranes, using a similar calculation method, the heat flux driven by flashing will be determined as  $q_{flh} = 5.92 \text{ W/cm}^2$ , which is still ~ 5% of the maximum interfacial heat flux. In addition to modeling, a baseline experiment was performed where a graduated cylinder containing IPA is placed in the chamber pumped down to 60 Pa. The liquid will evaporate with decreasing rate as it cools down and eventually stops evaporating at the saturation temperature of -20  $^{\circ}\text{C}$ . At the beginning of the process, the fastest evaporation rate was found to be ~ 1mL/min with the opening area of the cylinder measured to be 6.4  $\text{cm}^2$ . The evaporative heat flux was determined as  $733 \times 0.786 / 60 / 6.4 = 1.5 \text{ W/cm}^2$ , which is on the same order with model estimations. Therefore, we can conclude the flashing of the liquid is not significant in contributing to the heat transfer of the total evaporation process.

To place the experimental results in context, we also developed a model based on energy conservation to demonstrate the potential of our proposed configuration to achieve high heat fluxes shown in Fig. 24. The permeability of the membranes,  $\alpha$ , can be determined based on the heating power and driving pressure at the transition between the flooding and the thin film regimes in the experiments:  $\alpha = (\Delta P / L) / (\dot{q} / \rho h_{fg})$ , where  $\Delta P$  is the pressure difference across the membrane,  $L$  is the thickness of the membrane,  $\dot{q}$  is the interfacial heat flux,  $\rho$  is the liquid density, and  $h_{fg}$  is the latent heat of the fluid. Therefore, the maximum interfacial heat flux is inversely proportional to the thickness of the membrane,  $\dot{q} = \rho h_{fg} \Delta P / \alpha L$ , (solid lines in Fig.24). Using the experimentally determined permeabilities and capillary pressures of the 100  $\mu\text{m}$  and 50  $\mu\text{m}$  thick membranes, an upper and lower bound on the maximum interfacial heat fluxes were used due to the inevitable variability of the pore geometry during fabrication. The experimental results (diamond symbols) show good agreement with the model. If membrane thicknesses on the order of 1  $\mu\text{m}$  were used, the maximum interfacial heat fluxes could be as high as 5000  $\text{W/cm}^2$  with overall heat fluxes over 1000  $\text{W/cm}^2$  even with membrane porosities of  $\approx 24\%$ .

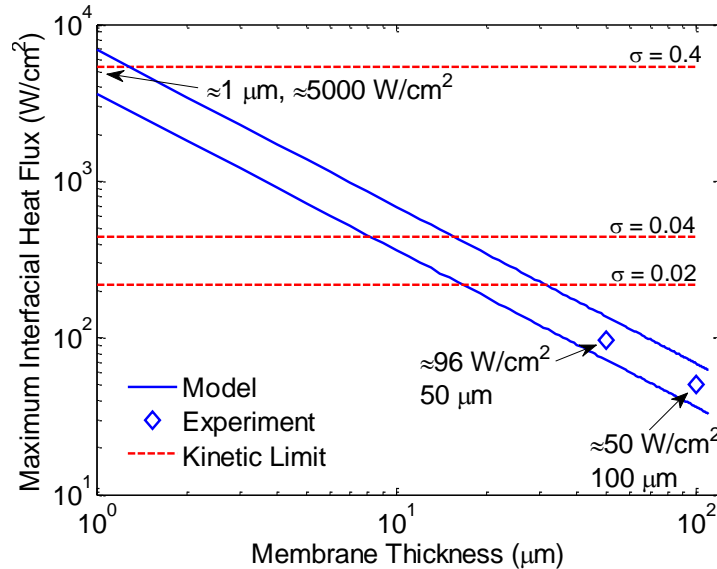


Fig. 24 Maximum interfacial heat fluxes dependent on both membrane thickness and accommodation coefficient. The inverse proportional relation between heat fluxes and thickness was validated by experimental results on 100 and 50  $\mu\text{m}$  membranes. By reducing the thickness and choosing fluid with higher accommodation coefficient, interfacial heat fluxes as high as 5000  $\text{W/cm}^2$  could be achieved.

In previous experiments, the maximum heat fluxes are only limited by the supply of the fluid, which is true in relatively lower heat fluxes. Under very high heat fluxes, however, kinetic theory needs to be considered in determining the maximum allowed heat flux [34]. Based on kinetic theory, the maximum heat flux across the interface can be determined as

$$q_i'' = \frac{2\hat{\sigma}}{2 - \hat{\sigma}} h_{fg} \sqrt{\frac{M}{2\pi R}} \left( \frac{p_{l,corr}}{\sqrt{T_l}} - \frac{p_v}{\sqrt{T_v}} \right) \quad (23)$$

where  $p_{l,corr}$  is the corrected liquid pressure based on Kelvin's equation where the curvature of the meniscus is accounted for

$$p_{l,corr} = p_l \exp\left(-\frac{2\gamma_{lv}M}{r_p R \rho_l}\right) \quad (24)$$

and  $\hat{\sigma}$  is the accommodation coefficient which describes the probability of a liquid molecule actually evaporates in contrast to reflect back to liquid phase. The value of the accommodation coefficient is highly sensitive to the purity of the system as well as the dynamic property of the fluid. For polar fluids such as ethanol, methanol, n-propyl alcohol, and water, the reported values of  $\hat{\sigma}$  are typically 0.02 to 0.04. For very pure non-polar fluids, such as benzene or carbon tetrachloride,  $\hat{\sigma}$  can be very close to 1 [35].

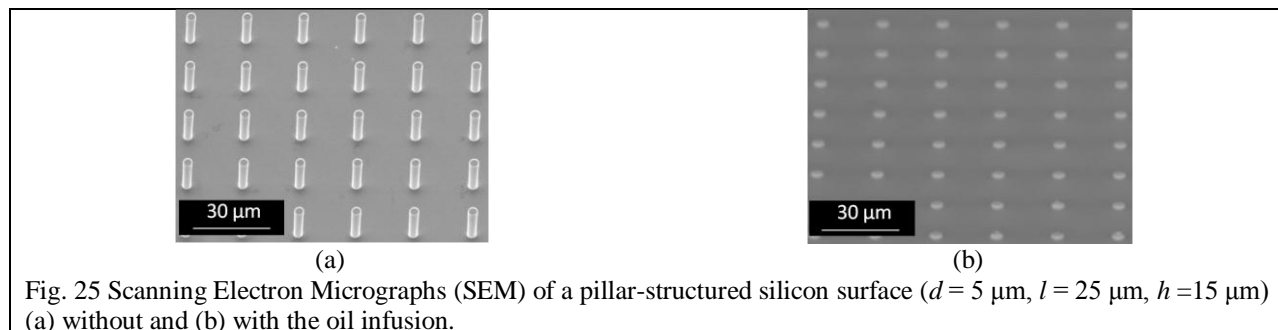
As shown with the membranes tested in previous experiments (50  $\mu\text{m}$  and 100  $\mu\text{m}$  thick), the interfacial heat fluxes were determined by the transport of liquid in the nanopores. The maximum demonstrated interfacial heat flux of 96  $\text{W}/\text{cm}^2$  is still well below the kinetic limit given accommodation coefficients in the range from 0.02 to 0.04. The results using the two kinds of membranes demonstrate the idea that the interfacial heat fluxes can be significantly enhanced by scaling down the membrane thickness. Considering the porosity of 24%, to dissipate heat flux over 1000  $\text{W}/\text{cm}^2$  would require interfacial heat fluxes as high as 5000  $\text{W}/\text{cm}^2$ . Under such high heat fluxes, kinetic limit must be considered where ultra pure non-polar fluid with accommodation coefficients larger than 0.4 will be required as well as membrane thickness  $\sim 1 \mu\text{m}$ . However, aluminium oxide membranes with thickness smaller than 50  $\mu\text{m}$  are very flimsy and cannot sustain the large pressure difference in the experiments. Future actual devices targeting heat fluxes above 1000  $\text{W}/\text{cm}^2$  would need supporting structures to enhance the mechanical integrity of the thin membranes.

#### 4) Increased Nucleation Density on Oil-Infused Superhydrophobic Surface for Enhanced Condensation Heat Transfer

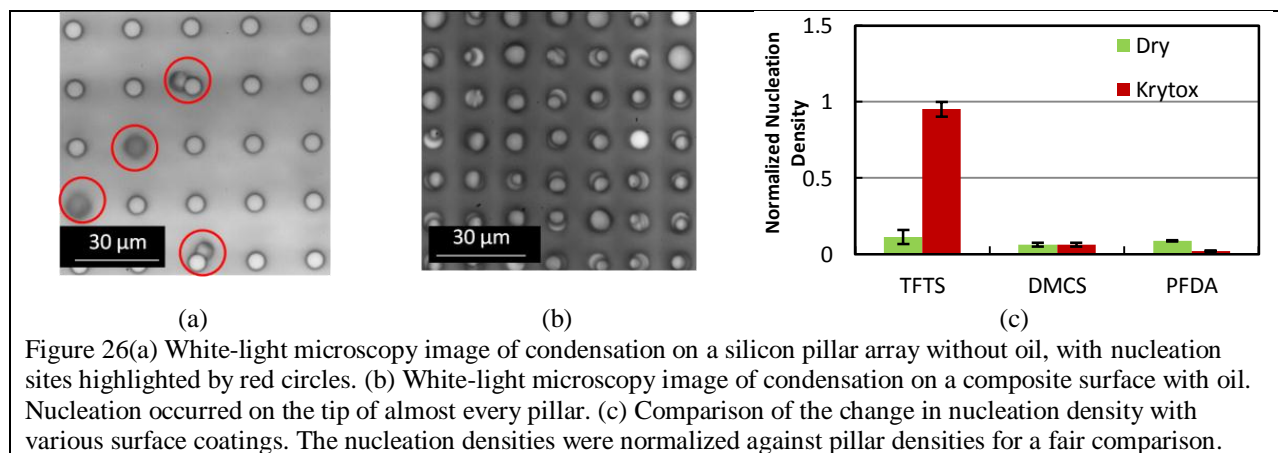
In this work, we showed that the nucleation density on oil-infused, silane-coated structured surfaces can be significantly increased by the use of disordered long-chain silane coatings that result in nucleation sites limited only by the density of pillar structures comprising the surface. We find that the increase in the nucleation density can be explained by heterogeneity in the surface energy of the silane coating and the reduced water-oil interfacial energy. This effect could potentially be used to significantly improve the heat transfer coefficient in condensation by controlling the nucleation density.

Well-defined silicon micro/nanopillar arrays with diameters,  $d$ , ranging from 0.4  $\mu\text{m}$  to 5  $\mu\text{m}$ , periods,  $l$ , ranging from 4  $\mu\text{m}$  to 25  $\mu\text{m}$ , and heights,  $h$  ranging from 10  $\mu\text{m}$  to 25  $\mu\text{m}$  were used in our experiments. The silicon surfaces were functionalized with three different chemicals: 1) (Tridecafluoro-1,1,2,2-tetrahydrooctyl)-1-trichlorosilane (TFTS) [UCT Specialties], which forms a self-assembled coating (SAC) by chemical vapor deposition (CVD) with a relatively long carbon chain (MW = 481.54 g/mol), 2) Dimethyldichlorosilane (DMCS) [Sigma-Aldrich], which forms a self-assembled monolayer (SAM) by CVD with a short carbon chain (MW = 129.06 g/mol), and 3) Poly(1H, 1H, 2H, 2H-perfluorodecyl acrylate) (PFDA) polymer, which was deposited using initiated chemical vapor deposition (iCVD) with a typical film thickness of 35 nm. Goniometric measurements on smooth functionalized silicon surfaces showed advancing and receding contact angles of:  $\theta_a/\theta_r = 122^\circ \pm 1.3^\circ/78^\circ \pm 1.3^\circ$  (equilibrium contact angle  $\theta_e \approx 102.1^\circ \pm 0.9^\circ$ );  $\theta_a/\theta_r = 103.8^\circ \pm 0.5^\circ/102.7^\circ \pm 0.4^\circ$  ( $\theta_e \approx 103.2^\circ \pm 0.3^\circ$ ); and  $\theta_a/\theta_r = 121.1^\circ \pm$

$2.2^\circ/106.3^\circ \pm 2.4^\circ$  ( $\theta_c \approx 113.5^\circ \pm 1.6^\circ$ ) for deposited films of TFTS, DMCS, and PFDA respectively. A small droplet of Krytox GPL 100 oil [DuPont] was applied to the functionalized silicon pillar arrays. The surface tension of Krytox oil is  $\sim 17$ - $19$  mN/m, allowing the oil to spread on the surface. A dry nitrogen stream was used to assist spreading and remove excess oil. Typical scanning electron micrographs (SEM) of the silicon pillar arrays without and with the oil are as shown in Fig. 25(a) and (b).



We investigated the nucleation behavior on the surfaces with and without the oil under white light optical microscopy (OM). The samples were horizontally mounted on a thermal stage [Instec Inc.] inside an enclosure and cooled to  $T_w = 283.1 \pm 0.1\text{K}$  in a dry nitrogen atmosphere. Following thermal equilibration ( $\sim 5$  min), nucleation was initiated by flowing water-saturated nitrogen into the enclosure. The supersaturation, defined as the ratio of the vapor pressure to the saturation pressure at the stage temperature ( $p_v/p_w$ ), was controlled by the temperature of the water reservoir through which the nitrogen carrier gas was sparged and measured using a humidity probe [Hygroclip, Rotronic] located  $\sim 1$  cm above the sample. Typical values of the supersaturation were around  $S \approx 1.6$ . The nucleation density and subsequent growth behavior was recorded at a frame rate of 30 fps using a CMOS camera [Phantom V7.1, Vision Research] attached to the optical microscope. As shown in Fig. 26 (a) and (b), the nucleation density on oil-infused surface with long-chain TFTS coating was significantly higher than that on the same surface without oil. We did not observe any nucleation between pillars which can be attributed to the large thickness of oil coverage between pillars that introduces a large diffusion resistance for water vapor. However, a droplet was formed on the tip of almost each pillar where the oil film was thin enough to allow sufficient mass to diffuse to the functionalized silicon surface. Meanwhile, on pillar arrays coated with DMCS and PFDA, we did not observe similar increases in nucleation density, as shown in Fig. 26(c).



To investigate the mechanism for this drastic change in nucleation density, we performed atomic force microscopy (AFM) in tapping mode on a smooth TFTS-coated silicon surface and observed the presence of nanoscale agglomeration of silane molecules, as shown in Fig. 27(a). Such agglomerates have been



observed in previous studies and considered as disordered agglomeration of excessive silane molecules [36]. The phase image of the AFM measurement (Fig. 27(d)) showed significantly higher phase angle on the agglomerates, which suggests that the agglomerates were locally more hydrophilic compared to the background film. Such heterogeneity was also supported by the high contact angle hysteresis ( $\theta_a / \theta_r = 122^\circ \pm 1.3^\circ / 78^\circ \pm 1.3^\circ$ ). However, such agglomerates were not observed on other kinds of surface coatings such as DMCS and PFDA, as shown in Fig. 27(b) and (c).

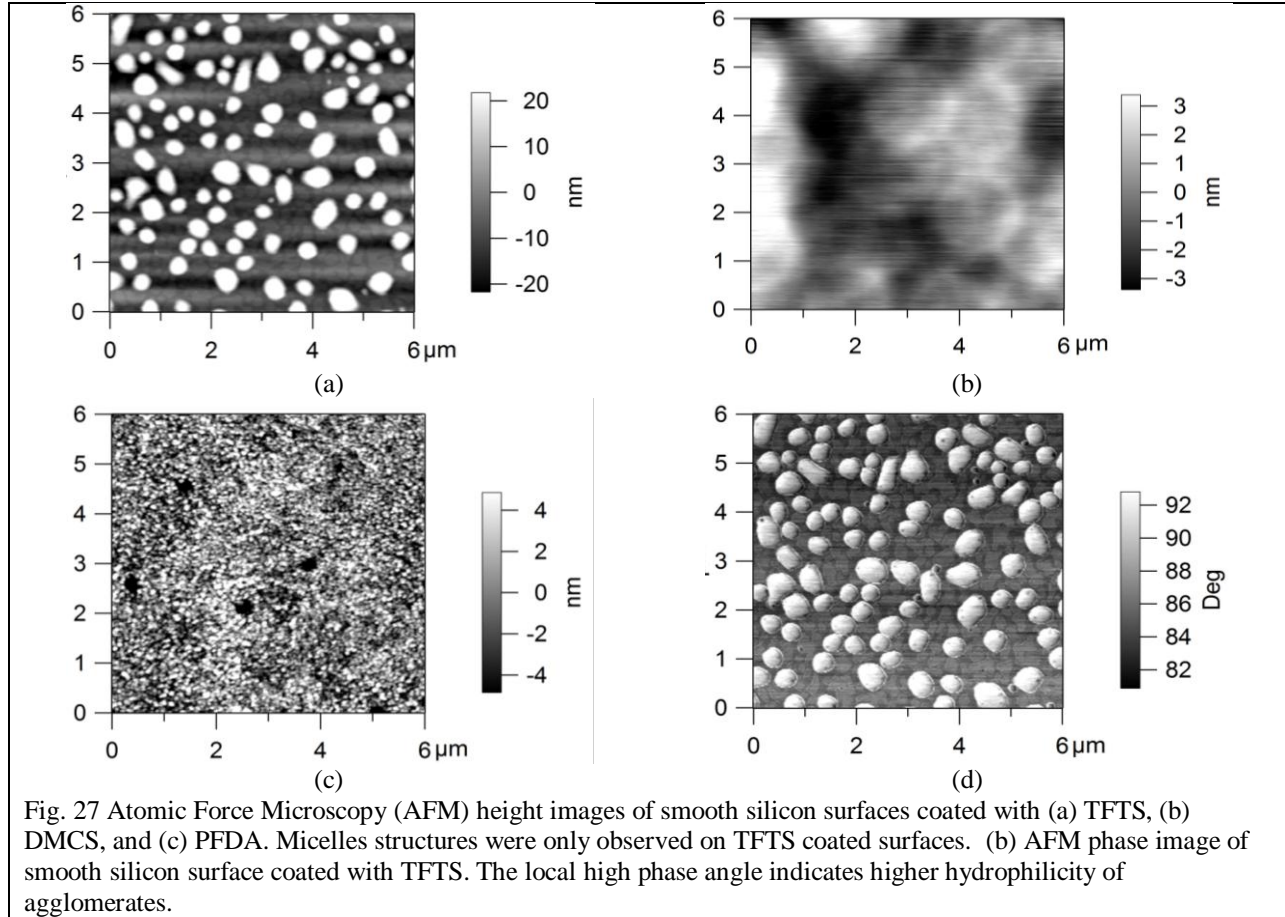


Fig. 27 Atomic Force Microscopy (AFM) height images of smooth silicon surfaces coated with (a) TFTS, (b) DMCS, and (c) PFDA. Micelles structures were only observed on TFTS coated surfaces. (b) AFM phase image of smooth silicon surface coated with TFTS. The local high phase angle indicates higher hydrophilicity of agglomerates.

The local contact angles on the hydrophobic substrate and the nanoscale agglomerates can be determined based on a modified Cassie-Baxter model. Assuming the local contact angles on the hydrophobic substrate and the nanoscale agglomerates to be  $\theta_1$  and  $\theta_2$ , respectively, the macroscopic advancing and receding contact angles are determined as

$$\theta_a = \theta_1 \quad (25)$$

$$\cos\theta_r = \sqrt{f}\cos\theta_2 + (1 - \sqrt{f})\cos\theta_1 \quad (26)$$

where  $f$  is the area fraction of the agglomerates [37].

Based on the macroscopically measured advancing and receding angles,  $\theta_a = 122^\circ \pm 1.3^\circ$  and  $\theta_r = 78^\circ \pm 1.3^\circ$ , and the fraction of the agglomerates determined as  $f \approx 0.4$  from AFM, the local contact angles on the hydrophobic substrate and the hydrophilic micelles were found to be  $\theta_1 = 122^\circ \pm 1.3^\circ$  and  $\theta_2 = 60^\circ \pm 1.5^\circ$ .

The nucleation rate,  $J$ , can be determined by classical nucleation theory (CNT) as [38]

$$J = zf^* \exp(-G^*) \quad (27)$$

In Eqn. (24),  $z$  is the Zeldovich factor and  $G^*$  is the dimensionless energy barrier, given by

$$z = (kT \ln S)^2 / 8\pi v_o \sqrt{kT\psi(\theta)\gamma^3} \quad (28)$$

$$G^* = 16\pi\psi(\theta)v_o^2\gamma^3/3(kT)^2 (\ln S)^2 \quad (29)$$

where  $S$  is the supersaturation and  $\psi(\theta)$  is the activity that accounts for the effect of contact angle.  $f^*$  is the frequency of monomer attachment to the critical droplet nucleus dependent on the nature of the nucleus growth. The main modes of growth during heterogeneous nucleation are limited *via* surface diffusion or direct impingement of monomers to the nucleus [39, 40]. Volumetric diffusion is a third growth limiting step, which is only considered important for nucleation taking place in liquid or solid solutions [6]. However, we included all three mechanisms when calculating the nucleation rates.

The frequency of monomer attachment due to direct vapor impingement is given by

$$f^*_i = \gamma_n [(1 - \cos(\theta_w))/2\psi^{2/3}(\theta)] (36\pi v_o^2)^{1/3} I n^{2/3} \quad (30)$$

where  $\gamma_n$  is the sticking coefficient ( $0 < \gamma_n < 1$ ),  $I$  is the classical Hertz-Knudsen impingement rate ( $I = P/\sqrt{2\pi m_o kT}$ ),  $n$  is the number of molecules in the nucleated cluster, and  $v_o$  is the volume of an individual water molecule ( $v_o = 3 \times 10^{-29} \text{ m}^3$ ). To determine an upper bound on the nucleation rate, a sticking coefficient of one was assumed ( $\gamma_n = 1$ ).

The frequency of monomer attachment due to surface diffusion is given by  $f^*_{sd} = \gamma_n c^* \lambda_s^2 I$ , where  $c^*$  is the capture number due to surface diffusion ( $1 < c^* < 5$ ), and  $\lambda_s$  is the mean surface diffusion distance of an adsorbed monomer on the substrate. The capture number  $c^*$  is size independent and approximately equal to 1.9 for heterogeneous condensation of water vapor [41]. The mean surface diffusion distance is dependent on the wettability of the substrate and is given by  $\lambda_s = \sqrt{D_{sd}\tau_d}$  where  $D_{sd}$  is the surface diffusion coefficient ( $D_{sd} = d_s^2 v_s \exp[-E_{sd}/kT]$ ),  $\tau_d$  is the desorption time ( $\tau_d = (1/v_s) \exp[-E_{des}/kT]$ ),  $v_s$  is the adsorbed molecule vibration frequency determined using the Debye approximation ( $v_s = V_D a/2$ ),  $d_s$  is the length of a molecular jump along the substrate surface approximated by the lattice constant of the substrate ( $d_s = 5.4 \text{ \AA}$ ) [42] and  $V_D$  is the speed of sound in the substrate ( $V_D = 8433 \text{ m/s}$ ). The desorption and surface diffusion energies are given by  $E_{des} = E_1 + \sigma_{sv} a_o$  and  $E_{sd} = 0.5E_{des}$ , respectively, where  $E_1$  is the binding energy of an  $n = 1$  sized cluster,  $\sigma_{sv}$  is the solid vapour interfacial energy and  $a_o$  is the water molecule surface area ( $a_o = 4.67 \times 10^{-19} \text{ m}^2$ ). The calculated energies of desorption show excellent agreement with that of experiment and molecular dynamics simulations ( $E_{des, SiO_2} = 0.9 \text{ eV}$ ) [43].

The frequency of monomer attachment due to volumetric diffusion is given by

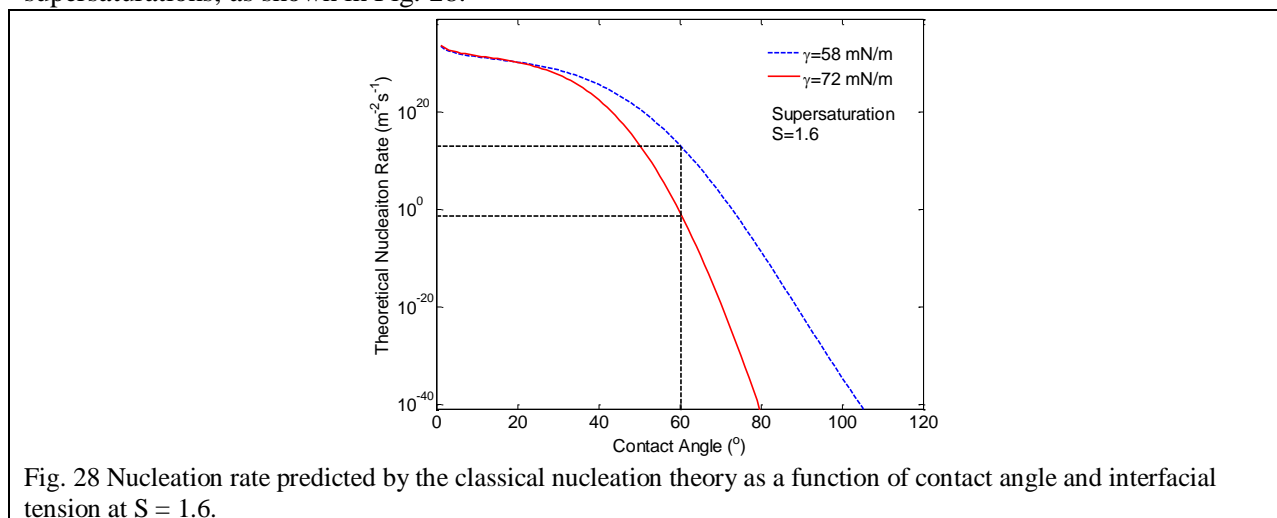
$$f^*_{vd} = \gamma_n \left(1 - \frac{\cos \theta_w}{\psi^{1/3}}\right) (6\pi^2 v_o)^{1/3} D C n^{1/3} \quad (31)$$

where  $D$  is the self diffusion coefficient of water vapor ( $D = (3/8\pi n_o d_o^2) \sqrt{kT/\pi m_o}$ ),  $C$  is the equilibrium concentration of monomers ( $C = (1/a_o) \exp(-W_1/kT)$ ),  $d_o$ ,  $m_o$  and  $n_o$  are the water molecule diameter ( $d_o = 3.0 \text{ \AA}$ ) [43], mass ( $m_o = 3 \times 10^{-26} \text{ kg}$ ) and number density ( $n_o = N_A/v_M$ ), respectively.

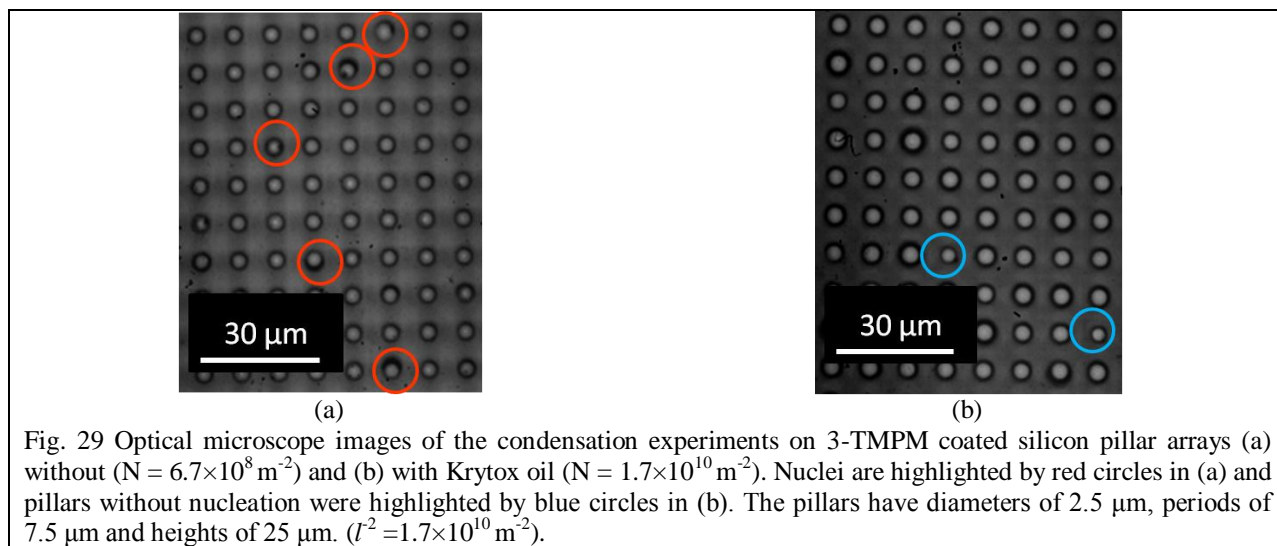
By adding the nucleation rate from the three mechanisms together, the nucleation rate,  $J$ , can be determined as a function of the contact angle and surface tension of the condensate at given



supersaturations, as shown in Fig. 28.



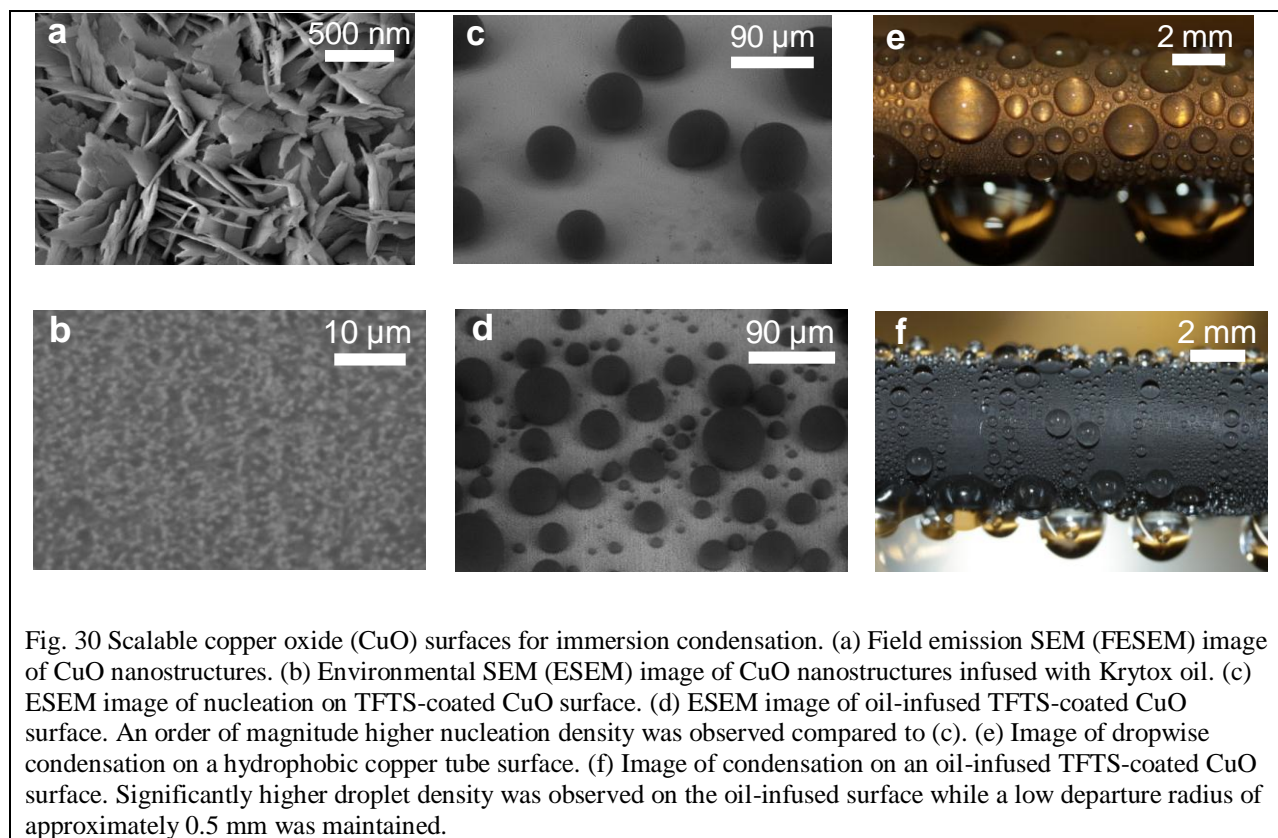
The surface tension of water in air is 72 mN/m and the interfacial tension between water and the Krytox oil was found to be 58 mN/m by measuring the contact angle of water droplet on oil film. From Fig. 28 we can see that for the hydrophilic micelles ( $\theta \approx 60^\circ$ ), the reduced interfacial tension between water and oil leads to a significant increase in the nucleation rate. With the nanoscale agglomerates acting as nucleation sites, nucleation was supposed to occur on almost every pillar tip where the oil film was thin enough for water vapor to diffuse through. On surfaces without the agglomerates, such as DMCS and PFDA-coated surfaces, the contact angles are over  $100^\circ$  and the nucleation rate was essentially zero even with reduced interfacial tension.



In order to validate our assumption, we carried out condensation experiments using silicon pillar arrays coated with 3-(trimethoxysilyl)propyl methacrylate (3-TMPM). The advancing and receding contact angle of water on a smooth silicon surface coated with 3-TMPM are  $65^\circ \pm 1.5^\circ$  and  $53^\circ \pm 1.1^\circ$ , respectively. The contact angle is in the range where the nucleation rate will be almost zero with a surface tension of 72 mN/m and nucleation should occur on every tip of pillars with an interfacial tension of 58 mN/m. Optical images of the condensation experiments are as shown in Fig. 29. Similar to the behavior of TFTS-coated surface, a significant increase in nucleation density was observed with the addition of

Krytox oil as expected. This result supports well our hypothesis related to the role of the hydrophilic nanoscale agglomerates in the droplet nucleation process.

Next, we studied the overall heat transfer performance of an immersion condensation surface. While studies on well-defined silicon micropillar arrays can provide physical insight into immersion condensation behavior, they are not practical due to cost and challenges in interfacing the silicon substrate and our heat transfer measurement apparatus with minimum uncertainties. Therefore, we performed immersion condensation heat transfer measurements on oil-infused copper oxide (CuO) nanostructures functionalized with TFTS, which promises a scalable, low cost platform for condensation surfaces.[30] SEM images of representative copper oxide nanostructures without and with Krytox oil-infusion are shown in Fig. 30a & b, respectively. Condensation experiments were performed on the CuO surfaces without and with oil-infusion in an environmental SEM with  $1 < S < 1.29$  for visualization.[12] The Figures 30c & d show an order of magnitude increase in nucleation density on the oil-infused surface, as similarly observed on the silicon-based microstructures. To capture the condensation heat transfer behavior, we formed the oil-infused heterogeneous CuO surfaces on copper tubes (see Methods for detailed fabrication process). Figures 30e & f show condensation on a typical hydrophobic surface and an oil-infused heterogeneous surface, respectively. Significantly higher droplet densities were observed on the oil-infused surface, while a low departure radius of approximately 0.5 mm was maintained. Prior to droplet departure, the droplets grew orders of magnitude larger than the characteristic length scale of the nanostructures, thus high apparent contact angles of the droplet ( $\approx 110^\circ$ ) were observed, consistent with the low surface energy of the solid-oil composite surface.



Overall heat transfer coefficients were measured to evaluate the performance on three different CuO-based surfaces: a hydrophobic surface for typical dropwise condensation (DHP), a superhydrophobic

TFTS-coated copper oxide surface (SHP), and a Krytox oil-infused, TFTS-coated CuO surface (Fig. 31). The Krytox GPL 100 oil evaporates completely when the test chamber is evacuated to pressures lower than 1 Pa. Therefore, we set the initial chamber pressure as high as 30 Pa (primarily composed of non-condensable gases, NCG) to avoid the evaporation of oil with steam pressures ranging from 2 to 3 kPa ( $1 < S < 1.6$ ) in the experiments. This is consistent with actual condenser systems where NCG partial pressures are typically found in the range of 30 Pa and significantly affect the condensation heat transfer performance.[44-47] Accordingly, with these experimental conditions, we were able to emulate a more realistic condensation environment and demonstrate the practical significance of the immersion condensation mode. While the SHP surface is more hydrophobic than the DHP surface, flooding and strong pinning of the condensate was observed due to the high supersaturation conditions ( $S$  as high as 1.6), leading to similar heat transfer coefficients with the DHP surfaces. Note that these results are distinct from previous literature where jumping of droplets on SHP surfaces increased heat transfer coefficients at lower saturation conditions ( $S < 1.12$ ).[48] In addition, the overall heat transfer coefficients on DHP surfaces in this work ( $h \approx 2\text{--}7 \text{ kW/m}^2\text{K}$ ) are much lower compared to pure vapor conditions ( $h \approx 12\text{--}13 \text{ kW/m}^2\text{K}$ )[48] due to the presence of NCGs acting as a diffusion barrier to the transport of water vapor towards the condensing surface. In comparison to the DHP surfaces, the Krytox oil-infused TFTS-coated CuO surface demonstrated approximately a 100% improvement in heat transfer coefficient over the entire range of supersaturations tested ( $1 < S < 1.6$ ) with the existence of NCGs. While the available condensation area was reduced due to the significant oil coverage, the significant improvement in the overall heat transfer coefficient highlights the collective role of enhanced nucleation density, more frequent droplet removal, and lower droplet contact angle.

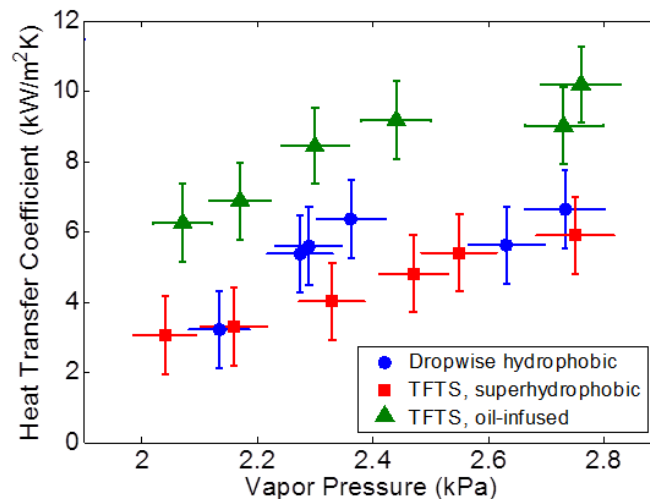


Fig. 31 Experimental immersion condensation heat transfer measurement. Comparison of overall heat transfer coefficient during condensation on the hydrophobic surface, TFTS-coated superhydrophobic surface, and oil-infused composite surface with 30 Pa of non-condensable gases. The supersaturation was varied in the range  $1 < S < 1.6$ . The heat transfer coefficient on the oil-infused surface increased by approximately 100% compared to the dropwise and superhydrophobic surfaces.

Oil-impregnated surfaces have been recently reported as a promising approach to enhance condensation heat transfer surfaces due to the ultra-low droplet adhesion.[49-51] However, easy droplet removal is not the only desired property for high heat transfer performance. Low contact angle and high nucleation densities are also essential for maximized condensation heat transfer. In this work, we have demonstrated that by combining surface heterogeneity and oil-infusion, the nucleation density in condensation can be increased by over an order of magnitude *via* immersion condensation while maintaining low droplet adhesion, which has never been observed previously. The increase in nucleation densities was achieved by a combined effect of heterogeneity and reduced oil-water interfacial tension as explained by our model

based on classical nucleation theory and the model was validated by control experiments using silane-coated silicon micropillar arrays. With improved understanding of the physics, we investigated oil-infused superhydrophobic copper oxide surfaces as a platform for condensation enhancement in practical systems. We demonstrated that the condensation heat transfer coefficient on such oil-infused heterogeneous surfaces can be enhanced by approximately 100% compared to state-of-the-art dropwise surfaces in the presence of non-condensables gases. Further work is needed to tailor oil and coating properties, as well as surface geometry to minimize oil loss during operation and maximize condensing surface area. With continued development, immersion condensation promises to be an important condensation mode for a variety of heat transfer and resource conserving applications.

## References

1. Mudawar, I., *Assessment of high-heat-flux thermal management schemes*. IEEE Transactions on Components & Packaging Technologies, 2001. **24**(2): p. 122-141.
2. Kandlikar, S.G. and A.V. Bapat, *Evaluation of jet impingement, spray and microchannel chip cooling options for high heat flux removal*. Heat Transfer Engineering, 2007. **28**(11): p. 911-923.
3. Garimella, S.V., *Advances in mesoscale thermal management technologies for microelectronics*. Microelectronics Journal, 2006. **37**(11): p. 1165-1185.
4. Bowers, M.B. and I. Mudawar, *High-flux boiling in low-flow rate, low-pressure drop mini-channel and microchannel heat sinks*. International Journal of Heat and Mass Transfer, 1994. **37**(2): p. 321-332.
5. Kandlikar, S.G., *Fundamental issues related to flow boiling in minichannels and microchannels*. Experimental Thermal and Fluid Science, 2002. **26**(2-4): p. 389-407.
6. Kandlikar, S.G., et al., *Stabilization of flow boiling in microchannels using pressure drop elements and fabricated nucleation sites*. Journal of Heat Transfer, 2006. **128**(4): p. 389-396.
7. Qu, W. and I. Mudawar, *Measurement and correlation of critical heat flux in two-phase micro-channel heat sinks*. International Journal of Heat and Mass Transfer, 2004. **47**(10/11): p. 2045-59.
8. Zhang, L., et al., *Phase Change Phenomena in Silicon Microchannels*. International Journal of Heat and Mass Transfer, 2005. **48**(8): p. 1572-1582.
9. Ohadi, M., J. Qi, and J. Lawler, *Ultra-Thin Film Evaporation (UTF) - Applications to Emergin Technologies in Cooling of Microelectronics*, in *Microscale Heat Transfer Fundamentals and Applications*, S. Kakaç, et al., Editors. 2005, Springer Netherlands. p. 321-338.
10. Wang, E.N., et al., *Micromachined Jets for Liquid Impingement of VLSI Chips*. Journal of MicroElectroMechanical Systems, 2004. **13**(5): p. 833-842.
11. Boreyko, J.B. and C.-H. Chen, *Self-Propelled Dropwise Condensate on Superhydrophobic Surfaces*. Physical Review Letters, 2009. **103**(18): p. 184501.
12. Miljkovic, N., R. Enright, and E.N. Wang, *Effect of Droplet Morphology on Growth Dynamics and Heat Transfer during Condensation on Superhydrophobic Nanostructured Surfaces*. Acs Nano, 2012. **6**(2): p. 1776-1785.
13. Chu, K.H., R. Xiao, and E.N. Wang, *Uni-directional spreading on asymmetric nanostructured surfaces*. Nature Materials, 2010. **9**: p. 413-417.
14. Xiao, R., K.H. Chu, and E.N. Wang, *Multilayer liquid spreading on superhydrophilic nanostructured surfaces*. Applied Physics Letters, 2009. **94**(19).
15. Brakke, K.A., *The Surface Evolver*. Experimental Mathematics, 1992. **1**(2): p. 141-165.
16. Wenzel, R.N., *Resistance of Solid Surfaces to Wetting by Water*. Ind. Eng. Chem., 1936. **28**(8): p. 988-994.
17. Sangani, A.S. and A. Acrivos, *Slow flow past periodic arrays of cylinders with application to heat transfer*. International Journal of Multiphase Flow, 1982. **8**(3): p. 193.
18. Quéré, D., *Wetting and roughness*. Annu. Rev. Mater. Res., 2008. **38**: p. 71-99.

19. Bico, J., U. Thiele, and D. Quéré, *Wetting of textured surfaces*. Colloids and Surfaces A: Physicochemical and Engineering Aspects, 2002. **206**(1-3): p. 41-46.
20. Patankar, N.A., *Transition between superhydrophobic states on rough surfaces*. Langmuir, 2004. **20**(17): p. 7097-7102.
21. Bico, J., C. Marzolin, and D. Quéré, *Pearl drops*. EPL (Europhysics Letters), 1999. **47**: p. 220.
22. Cassie, A. and S. Baxter, *Wettability of porous surfaces*. Trans. Faraday Soc., 1944. **40**(0): p. 546-551.
23. Peterson, G., *An Introduction to Heat Pipes: Modeling, Testing and Applications*, (1994), Wiley, New York.
24. Shanks, H., et al., *Thermal conductivity of silicon from 300 to 1400 K*. Physical Review, 1963. **130**(5): p. 1743.
25. Brinkman, H., *Applied Sci. Research A 1*, 27 (1947). Proc. Netherl. Acad. Sci. Amsterdam, 1947. **50**: p. 618.
26. Sangani, A. and A. Acrivos, *Slow flow past periodic arrays of cylinders with application to heat transfer*. International Journal of Multiphase Flow, 1982. **8**(3): p. 193-206.
27. Ranjan, R., J.Y. Murthy, and S.V. Garimella, *A microscale model for thin-film evaporation in capillary wick structures*. International Journal of Heat and Mass Transfer, 2011. **54**(1): p. 169-179.
28. Migliaccio, C., H. Dhavaleswarapu, and S. Garimella. *Microscale Temperature Measurements Near the Contact Line of an Evaporating Thin Film in a V-Groove*. 2009. ASME.
29. Dhavaleswarapu, H.K., et al., *Experimental investigation of evaporation from low-contact-angle sessile droplets*. Langmuir, 2009. **26**(2): p. 880-888.
30. Nam, Y. and Y.S. Ju, *Comparative Study of Copper Oxidation Schemes and Their Effects on Surface Wettability*. ASME Conference Proceedings, 2008. **2008**(48715): p. 1833-1838.
31. Mills, A.F., *Heat and Mass Transfer*. 2 ed. 1999: Prentice-Hall.
32. Wheeler, T.D. and A.D. Stroock, *The transpiration of water at negative pressures in a synthetic tree*. Nature, 2008. **455**(7210): p. 208-212.
33. Kandlikar, S.G., *A theoretical model to predict pool boiling CHF incorporating effects of contact angle and orientation*. TRANSACTIONS-AMERICAN SOCIETY OF MECHANICAL ENGINEERS JOURNAL OF HEAT TRANSFER, 2001. **123**(6): p. 1071-1079.
34. Carey, V.P., *Liquid-Vapor Phase-Change Phenomena*. 1992: Hemisphere Pub. Corp.
35. Paul, B., *Compilation of Evaporation Coefficients*. American Rocket Society Journal, 1962. **32**: p. 1321.
36. Bunker, B.C., et al., *The Impact of Solution Agglomeration on the Deposition of Self-Assembled Monolayers*. Langmuir, 2000. **16**(20): p. 7742-7751.
37. Raj, R., 2012.
38. Kashchiev, D., *Nucleation: Basic Theory with Applications*. 1 ed. 2000: Oxford: Butterworth-Heinemann.
39. Pound, G.M., M.T. Simnad, and L. Yang, *Heterogeneous Nucleation of Crystals from Vapor*. The Journal of Chemical Physics, 1954. **22**(7): p. 1215-1219.
40. Sigsbee, R.A., *Adatom Capture and Growth Rates of Nuclei*. Journal of Applied Physics, 1971. **42**(10): p. 3904-3915.
41. Pocker, D.J. and S.J. Hruska, *Detailed Calculations of the Number of Distinct Sites Visited in Random Walk on Several Two-Dimensional Substrate Lattices*. Journal of Vacuum Science and Technology, 1971. **8**(6): p. 700-707.
42. J.P.Hirth and G.M.Pound, *Condensation and evaporation - nucleation and growth kinetics* 1963: England: Pergamon Press.
43. Ma, Y., A.S. Foster, and R.M. Nieminen, *Reactions and clustering of water with silica surface*. The Journal of Chemical Physics, 2005. **122**(14): p. 144709-9.

44. Rose, J.W., *Dropwise condensation theory and experiment: A review*. Proceedings of the Institution of Mechanical Engineers, Part A: Journal of Power and Energy, 2002. **216**(2): p. 115-128.
45. Denny, V.E. and V.J. Jusionis, *Effects of noncondensable gas and forced flow on laminar film condensation*. International Journal of Heat and Mass Transfer, 1972. **15**(2): p. 315-326.
46. Sparrow, E.M., W.J. Minkowycz, and M. Saddy, *Forced convection condensation in the presence of noncondensables and interfacial resistance*. International Journal of Heat and Mass Transfer, 1967. **10**(12): p. 1829-1845.
47. Tanner, D.W., et al., *Heat transfer in dropwise condensation at low steam pressures in the absence and presence of non-condensable gas*. International Journal of Heat and Mass Transfer, 1968. **11**(2): p. 181-190.
48. Miljkovic, N., et al., *Jumping-Droplet-Enhanced Condensation on Scalable Superhydrophobic Nanostructured Surfaces*. Nano Letters, 2012.
49. Wong, T.-S., et al., *Bioinspired self-repairing slippery surfaces with pressure-stable omniphobicity*. Nature, 2011. **477**(7365): p. 443-447.
50. Anand, S., et al., *Enhanced Condensation on Lubricant Impregnated Nanotextured Surfaces*. Acs Nano, 2012.
51. Mishchenko, L., et al., *Design of Ice-free Nanostructured Surfaces Based on Repulsion of Impacting Water Droplets*. Acs Nano, 2010. **4**(12): p. 7699-7707.